

An accuracy analysis of Galerkin meshfree methods accounting for numerical integration

Junchao Wu^{a,b}, Dongdong Wang^{b,*}

^a College of Civil Engineering, Huaqiao University, Xiamen, Fujian 361021, China

^b Department of Civil Engineering, Xiamen University, Xiamen, Fujian 361005, China

Received 2 September 2020; received in revised form 23 November 2020; accepted 2 December 2020

Available online 25 December 2020

Abstract

Presently, it has been widely recognized that numerical integration plays a crucial role on the solution accuracy of Galerkin meshfree methods due to the rational nature of meshfree shape functions and the misalignment of shape function supports with integration cells. Nonetheless, the corresponding underlying cause is still not quite clear. To address this issue, an accuracy analysis of Galerkin meshfree methods is presented in this study with a special focus on the contribution of numerical integration to the error estimates. One important fact is that the integration difficulty of meshfree methods leads to a loss of the Galerkin orthogonality condition which usually serves as a basis to develop error bounds. In order to enable the accuracy analysis, an error measure is proposed to evaluate the loss of Galerkin orthogonality condition, which is actually related to the order of integration consistency for Galerkin meshfree formulation. With the aid of this orthogonality error measure, both H^1 and L^2 error estimates are established for Galerkin meshfree methods. It turns out that these errors essentially consist of two parts, one comes from the standard interpolation error, and the other one attributes to the numerical integration error. In accordance with the proposed error estimates, it is evident that for the conventional Gauss integration schemes violating the integration consistency, the solution errors eventually are controlled by the integration error and optimal convergence cannot be achieved even with high order quadrature rules. On the other hand, for the consistent integration approaches, e.g., the stabilized conforming nodal integration and the more recent reproducing kernel gradient smoothing integration, the integration and interpolation errors have the same accuracy order and thus an optimal convergence of Galerkin meshfree methods is ensured. The proposed theoretical error estimates for Galerkin meshfree methods are well demonstrated by numerical results.

© 2020 Elsevier B.V. All rights reserved.

Keywords: Meshfree method; Error estimate; Numerical integration; Integration consistency; Galerkin orthogonality; Reproducing kernel gradient smoothing integration

1. Introduction

Galerkin meshfree methods are one of the most popular classes of particle- or node-based numerical methods due to their strength on stability and accuracy [1–8]. Up to date, there are many types of versatile Galerkin meshfree methods have been proposed, for instance, diffuse element method [9], Element-free Galerkin method [10,11], reproducing kernel particle method [12,13], hp cloud method [14], partition of unity method [15], natural element

* Corresponding author.

E-mail address: ddwang@xmu.edu.cn (D. Wang).

method [16], meshless local Petrov–Galerkin [17], point interpolation method [18], reproducing kernel element method [19], max-entropy meshfree method [20,21], smoothed finite element method [22], semi-Lagrangian meshfree method [23], quasi-convex meshfree method [24], hierarchical partition of unity meshless method [25], quasi-linear reproducing kernel particle method [26], smoothed particle Galerkin method [27], and meshfree mimetic method [28], among others. More about the advances on meshfree methods can be found from the review article by Chen et al. [8]. Galerkin meshfree methods are realized by employing certain meshfree approximations within the Galerkin weak form. In contrast to the finite element polynomial shape functions, meshfree shape functions usually are not polynomials, for example, the frequently used moving least squares (MLS) [10,29] and reproducing kernel (RK) [12,13] meshfree approximations exhibit a rational nature. It turns out this rational approximation character of meshfree shape functions poses severe difficulty on the accurate numerical integration of Galerkin weak form.

As a natural extension of finite element formulation, Gauss integration has been used for the weak form evaluation of Galerkin meshfree methods through subdividing the problem domain into a set of integration cells, and then high order quadrature rules [30] are often employed in each cell to obtain satisfactory solution accuracy. Obviously, the use of high order quadrature rules will significantly lower the computational efficiency which is a major concern for numerical methods. However, here we shall show that high order quadrature rules can produce optimally convergent meshfree solutions only for relatively coarse discretizations and will eventually lose the desirable optimal convergence property as the discretizations are progressively refined. Besides the rational meshfree shape functions, the misalignment of shape function supports with integration cells introduces additional complexity on the numerical integration of Galerkin meshfree formulation [30]. Nodal integration is a straightforward choice to accelerate the meshfree computation, but it is often accompanied by the instability issue [31]. Adding stress points around the meshfree nodes [32–34] could enhance the stability of nodal integration but the computational efficiency is reduced in the meantime. Alternatively, a naturally stabilized meshfree nodal integration was realized through the efficient implicit gradient stabilization [35]. A virtual element decomposition was also presented to improve the consistency and stability of meshfree nodal integration with linear basis functions [36]. To match the support and integration domains, the support integration schemes [17,37–39] were proposed for meshfree methods, while very high order quadrature rules are still required in each support domain. Embarking from a different route, Chen et al. [40,41] identified the integration constraint for Galerkin meshfree methods and they showed that Gauss integration violates the integration constraint or integration consistency. Actually, the integration consistency of Galerkin meshfree methods is equivalent to passing the patch test in finite element analysis [42,43]. Consequently, a stabilized conforming nodal integration (SCNI) meeting the integration constraint was proposed by Chen et al. [40,41], where the costly direct derivative computation is avoided and both stability and efficiency are simultaneously achieved. Subsequently, SCNI has been successfully generalized and extended to various types of problems, e.g., thick and thin plates and shells [44–50], large deformation and failure analysis [51–56], etc. However, it is noted that SCNI was originally designed for the meshfree formulation with linear basis functions and only the linear exactness was emphasized therein [40].

An extension of SCNI to high order basis functions has been discussed by Duan et al. [57,58] and then a quadratically consistent meshfree integration algorithm (QCI) was proposed, which was later generalized to the strain gradient elasticity problems [59]. In this approach, the smoothed gradients of meshfree shape functions evaluated at Gauss points are obtained in accordance with the high order integration constraint. However, additional effort is required to solve systems of equations in each integration cell during the gradient evaluation. Meanwhile, Chen et al. [60,61] presented an arbitrary order variationally consistent integration (VCI), in which different integration schemes can be uniformly corrected to satisfy high order integration constraint through a redesign of the test functions. Nonetheless, this test function modification leads to a non-symmetric Petrov–Galerkin formulation. Based upon SCNI, Wang and Wu [62] introduced a nesting sub-domain gradient smoothing integration method, where the stiffness matrix is optimally sampled from two level triangular integration cells. But the generalization of this method to high order basis functions and three dimensional case is not straightforward. In order to develop efficient meshfree methods for high order basis functions, a reproducing kernel gradient smoothing integration (RKGSI) framework was recently presented by Wang and Wu [63,64]. According to RKGSI, reproducing kernel smoothed gradients of meshfree shape functions are built upon explicit quadrature rules whose number of sampling points are globally minimized. By construction, the integration consistency is an inherent property of RKGSI, and thus the traditional low order Gauss integration rules used in finite element analysis can be directly adopted for Galerkin meshfree formulation through replacing the standard gradients by the reproducing kernel smoothed gradients. It is noted that RKGSI recovers SCNI when linear basis functions are employed.

It has been thoroughly shown through numerical experiments that the aforementioned meshfree integration schemes meeting the integration constraint or integration consistency perform much better than the Gauss quadrature rules [8]. However, unlike the straightforward Gauss integration for finite element analysis with polynomial shape functions [65,66], the underlying theoretical mechanism for the numerical integration of Galerkin meshfree methods is still not quite clear. Liu et al. [67,68] introduced an interesting function analysis on the convergence of Galerkin meshfree methods. Chen et al. [69] proposed a new RK approximation with interpolation property, where the corresponding error analysis in Sobolev norm is also investigated. Han and Meng [70] provided a valuable accuracy analysis of Galerkin meshfree methods using reproducing kernel approximation, and the accuracy results are quite similar to those of the finite element analysis. However, these error estimates for Galerkin meshfree methods are purely bounded by the meshfree interpolation error, while the numerical integration effect is not considered therein. Babuška et al. [71] presented an investigation on the numerical integration error of stiffness matrix and force vector, but this error is not reflected in the final error estimates. An enhanced strain posteriori error estimator for SCNI was proposed by Rüter and Chen [72] for adaptive meshfree analysis, where the priori error estimates incorporating the numerical integration influence was also not touched. Consequently, it is highly desirable to clarify that how numerical integration affects the accuracy of Galerkin meshfree solutions from a theoretical point of view.

In this study, a theoretical accuracy analysis that takes into account the numerical integration is presented for Galerkin meshfree methods. The accuracy analysis of Galerkin formulation is often built upon the Galerkin orthogonality condition. However, this orthogonality condition is lost for Galerkin meshfree methods due to the inability to exactly evaluate the weak form via numerical integration. Thus in order to enable the accuracy analysis of Galerkin meshfree methods, an error estimate is firstly proposed to measure the error arising from the loss of Galerkin orthogonality. It turns out that the error in Galerkin orthogonality is closely related to the order of integration consistency. With the help of the error bound of Galerkin orthogonality, L^2 and H^1 error estimates are derived for Galerkin meshfree methods. It is shown that both L^2 and H^1 error estimates are formed by two constituents, one comes from the standard interpolation error of meshfree approximation that fully depends on the degree of basis functions, while another one attributes to the order of integration consistency that is determined by the integration schemes. According to these theoretical results, it is evident that the errors of Galerkin meshfree solutions are controlled by the interplay between the interpolation error and the integration error. For the Gauss integration approach violating the integration consistency condition, the solution errors will ultimately be dominated by the integration error rather than the interpolation error, and this issue cannot be fully resolved just through using high order quadrature rules. On the other hand, for the consistent integration schemes, e.g., SCNI, VCI, QC, and RKGSI, the optimal convergence of Galerkin meshfree formulation can be ensured since the order of integration consistency is the same as that of interpolation error. These theoretical results are demonstrated by numerical examples.

The remainder of this paper is organized as follows. Section 2 outlines the basic equations of Galerkin meshfree formulation. The numerical integration of Galerkin weak form is discussed in Section 3 with particular reference to the standard Gauss integration that violates the integration consistency and the reproducing kernel gradient smoothing integration that meets the integration consistency. A direct consequence of the numerical integration of Galerkin weak form, the loss of Galerkin orthogonality is also illustrated in Section 3. Subsequently, an error estimate to measure the loss of Galerkin orthogonality is proposed in Section 4, which is then used to derive both L^2 and H^1 error estimates for Galerkin meshfree methods. Numerical results are presented in Section 5 to demonstrate the effectiveness of the proposed theoretical accuracy measures. Finally, conclusions are given in Section 6.

2. Galerkin meshfree formulation

2.1. MLS/RK meshfree approximation

In this work, the Galerkin meshfree methods particularly refer to the Galerkin formulation with moving least squares (MLS) and reproducing kernel (RK) approximants, and it is noted that MLS and RK meshfree shape functions actually are identical when monomial basis functions are used. Consider an open and bounded problem domain Ω in n_{sd} -dimensional Euclidean space $\mathbb{R}^{n_{sd}}$ with Lipschitzian boundary $\partial\Omega$, a meshfree discretization of $\overline{\Omega} = \Omega \cup \partial\Omega$ is realized by a set of nodes or particles $\{\mathbf{x}_I\}_{I=1}^{n_p}$, where n_p denotes the total number of nodes. A MLS/RK meshfree approximant of a scalar field variable $u(\mathbf{x})$, denoted by $u^h(\mathbf{x})$, can be expressed as follows:

$$u^h(\mathbf{x}) = \sum_{I \in S(\mathbf{x})} \Psi_I(\mathbf{x}) d_I \quad (1)$$

where Ψ_I is the meshfree shape function associated with the node \mathbf{x}_I and it has a local and compact support $supp(\Psi_I)$ such that $\bar{\Omega} \subseteq \cup_{I=1}^{n_p} supp(\Psi_I)$, and $supp(\Psi_I)$ is characterized by the support size s_I . d_I is the corresponding nodal coefficient related with Ψ_I . $\mathcal{S}(\mathbf{x})$ stands for the set of nodes whose supports or influence domains cover the location \mathbf{x} , i.e., $\mathcal{S}(\mathbf{x}) = \{I | \mathbf{x} \in supp(\Psi_I)\}$. For convenience of subsequent development, we also define the following meshfree space V^h :

$$V^h = span\{\Psi_I(\mathbf{x})\}_{I=1}^{n_p} \quad (2)$$

In accordance with the reproducing kernel approximation theory [12,13], the meshfree shape function $\Psi_I(\mathbf{x})$ takes the following form:

$$\Psi_I(\mathbf{x}) = \mathbf{p}^T(\mathbf{x}_I - \mathbf{x})\mathbf{c}(\mathbf{x})\phi(\mathbf{x}_I - \mathbf{x}) \quad (3)$$

in which $\mathbf{p}(\mathbf{x})$ is the p th order monomial basis function vector:

$$\mathbf{p}^T(\mathbf{x}) = \{\varphi_{ijk}\} = \{1, x, y, z, \dots, x^i y^j z^k, \dots, z^p\}, \quad \varphi_{ijk} = x^i y^j z^k, 0 \leq i + j + k \leq p \quad (4)$$

$\mathbf{c}(\mathbf{x})$ is an unknown coefficient vector, $\phi(\mathbf{x}_I - \mathbf{x})$ is the kernel function that attributes to the continuity and locality of meshfree shape function Ψ_I . In this study, the widely used cubic B-spline function [1] is adopted as the kernel function, which can be conveniently generalized for multi-dimensional cases through the tensor product rule:

$$\phi(\mathbf{x}_I - \mathbf{x}) = \prod_{i=1}^{n_{sd}} \phi(r_i), \quad r_i = \frac{|\mathbf{x}_I - \mathbf{x}|}{s_{iI}} \quad (5)$$

with

$$\phi(r_i) = \begin{cases} \frac{2}{3} - 4r_i^2 + 4r_i^3 & r_i \leq \frac{1}{2} \\ \frac{4}{3} - 4r_i + 4r_i^2 - \frac{4}{3}r_i^3 & \frac{1}{2} < r_i \leq 1 \\ 0 & r_i > 1 \end{cases} \quad (6)$$

where s_{iI} denotes the support size in the i th direction.

The unknown coefficient vector $\mathbf{c}(\mathbf{x})$ is determined by imposing the so-called reproducing or consistency conditions [12,13]:

$$\sum_{I \in \mathcal{S}(\mathbf{x})} \Psi_I(\mathbf{x})\mathbf{p}(\mathbf{x}_I) = \mathbf{p}(\mathbf{x}) \quad (7)$$

or equivalently:

$$\sum_{I \in \mathcal{S}(\mathbf{x})} \Psi_I(\mathbf{x})\mathbf{p}(\mathbf{x}_I - \mathbf{x}) = \mathbf{p}(\mathbf{0}) \quad (8)$$

Plugging Eq. (3) into Eq. (8) yields:

$$\mathbf{A}(\mathbf{x})\mathbf{c}(\mathbf{x}) = \mathbf{p}(\mathbf{0}) \quad (9)$$

where \mathbf{A} is the moment matrix defined by:

$$\mathbf{A}(\mathbf{x}) = \sum_{I \in \mathcal{S}(\mathbf{x})} \mathbf{p}(\mathbf{x}_I - \mathbf{x})\mathbf{p}^T(\mathbf{x}_I - \mathbf{x})\phi(\mathbf{x}_I - \mathbf{x}) \quad (10)$$

As a result of Eq. (9), we get $\mathbf{c}(\mathbf{x}) = \mathbf{A}^{-1}(\mathbf{x})\mathbf{p}(\mathbf{0})$ and the meshfree shape function of Eq. (3) then becomes:

$$\Psi_I(\mathbf{x}) = \mathbf{p}^T(\mathbf{0})\mathbf{A}^{-1}(\mathbf{x})\mathbf{p}(\mathbf{x}_I - \mathbf{x})\phi(\mathbf{x}_I - \mathbf{x}) \quad (11)$$

According to Eq. (7), the meshfree shape functions also meet the following gradient reproducing conditions:

$$\sum_{I \in \mathcal{S}(\mathbf{x})} \Psi_{I,i}(\mathbf{x})\mathbf{p}(\mathbf{x}_I) = \mathbf{p}_{,i}(\mathbf{x}) \quad (12)$$

where the subscript comma denotes the partial differentiation operation with respect to the spatial coordinate x_i .

From Eq. (11), it is clear that meshfree shape functions are bounded in case that the moment matrix \mathbf{A} is invertible, which implies that the cardinality of $\{\mathbf{x}_I\}_{I \in \mathcal{S}(x)}$ should be greater than or equal to the dimension of basis vector \mathbf{p} defined by Eq. (4):

$$\text{card}\{\mathbf{x}_I\}_{I \in \mathcal{S}(x)} \geq \dim\{\mathbf{p}\} \quad (13)$$

If the nodal distribution meets the above condition throughout the problem domain, this meshfree discretization $\{\mathbf{x}_I\}_{I=1}^{n_p}$ is called (s, p) -regular [67], where p represents the degree of basis functions, s denotes a characterized length measuring the support size:

$$C_0 \leq \frac{s_I}{s} \leq C_1 \quad (14)$$

for some constants C_0 and C_1 . For $u \in C^m(\Omega)$, the meshfree interpolation error estimate in the Sobolev spaces of $H^l(\Omega)$ is given by [67]:

$$\|u - \mathcal{I}^p u\|_{H^l} \leq C s^{k-l+1} |u|_{H^{k+1}}, \quad \forall l \leq k+1, k = \min\{p, m\} \quad (15)$$

where $\mathcal{I}^p u$ stands for the meshfree interpolant of u , C is a constant related to operator \mathcal{I} .

2.2. Galerkin meshfree discretization

Without loss of generality, for clarity we consider the following scalar-valued potential problem as a model problem:

$$\begin{cases} -\Delta u = b, & \text{in } \Omega \\ u = g, & \text{on } \partial\Omega \end{cases} \quad (16)$$

where Δ denotes the Laplace operator, b is a given source term in $L^2(\Omega)$.

In Galerkin formulation, the strong form of Eq. (16) is converted to the following variational or weak form:

$$\text{Find } u \in H^1(\Omega): \mathcal{A}(v, u) = \mathcal{F}(v), \quad \forall v \in H^1(\Omega) \quad (17)$$

where $\mathcal{A}: H^1 \times H^1 \rightarrow \mathbb{R}$ is a bilinear form and $\mathcal{F}: H^1 \rightarrow \mathbb{R}$ is a linear form. Since meshfree shape functions usually do not have the interpolatory property, the Nitsche's method [73] is adopted herein to enforce the essential boundary condition. Accordingly, \mathcal{A} and \mathcal{F} in Eq. (17) are given by:

$$\mathcal{A}(v, u) = \int_{\Omega} \nabla v \cdot \nabla u d\Omega - \int_{\partial\Omega} (\mathbf{n} \cdot \nabla v) u d\Gamma - \int_{\partial\Omega} v (\mathbf{n} \cdot \nabla u) d\Gamma + \beta \int_{\partial\Omega} v u d\Gamma \quad (18)$$

$$\mathcal{F}(v) = \int_{\Omega} v b d\Omega - \int_{\partial\Omega} (\mathbf{n} \cdot \nabla v) g d\Gamma + \beta \int_{\partial\Omega} v g d\Gamma \quad (19)$$

in which ∇ is the gradient operator, $\mathbf{n} = \{n_i\}$ is the outward normal vector of $\partial\Omega$. Following the Lax–Milgram lemma [74], β in Eqs. (18) and (19) is a stabilized constant to ensure the coercivity of the bilinear form:

$$\mathcal{A}(v, v) \geq \alpha \|v\|_{H^1}^2, \quad \forall v \in H^1(\Omega) \quad (20)$$

Meanwhile, \mathcal{A} is also continuous:

$$|\mathcal{A}(v, w)| \leq \gamma \|v\|_{H^1} \|w\|_{H^1}, \quad \forall v, w \in H^1(\Omega) \quad (21)$$

where α, γ are two positive constants.

Subsequently, introducing the meshfree approximation of Eq. (1) into the variational problem of Eq. (17) along with Eqs. (18) and (19) gives:

$$\text{Find } u^h \in V^h: \mathcal{A}(v^h, u^h) = \mathcal{F}(v^h), \quad \forall v^h \in V^h \quad (22)$$

where v^h is the meshfree approximation of the test function v . A standard variational argument then leads to the following discrete meshfree equation:

$$\mathbf{K} \mathbf{d} = \mathbf{f} \quad (23)$$

where \mathbf{d} is nodal coefficient vector. \mathbf{K} and \mathbf{f} are the stiffness matrix and force vector, and their components are given by:

$$K_{IJ} = \int_{\Omega} \nabla \Psi_I \cdot \nabla \Psi_J d\Omega - \int_{\partial\Omega} \Psi_I (\mathbf{n} \cdot \nabla \Psi_J) d\Gamma - \int_{\partial\Omega} (\mathbf{n} \cdot \nabla \Psi_I) \Psi_J d\Gamma + \beta \int_{\partial\Omega} \Psi_I \Psi_J d\Gamma \quad (24)$$

$$f_I = \int_{\Omega} \Psi_I b d\Omega - \int_{\partial\Omega} (\mathbf{n} \cdot \nabla \Psi_I) g d\Gamma + \beta \int_{\partial\Omega} \Psi_I g d\Gamma \quad (25)$$

A combination of Eqs. (17) and (22) immediately gives to the orthogonality condition or best approximation property for Galerkin formulation:

$$\mathcal{A}(v^h, e) = 0, \quad \forall v^h \in V^h \quad (26)$$

where $e = u - u^h$. Moreover, we also have the following result:

$$\begin{aligned} \alpha \|e\|_{H^1(\Omega)}^2 &\leq |\mathcal{A}(e, e)| && \text{(Coercivity)} \\ &= \left| \mathcal{A}(u - u^h, e) + \underbrace{\mathcal{A}(u^h - \mathcal{I}^p u, e)}_{=0} \right| && \text{(Orthogonality)} \\ &= |\mathcal{A}(u - \mathcal{I}^p u, e)| && \text{(Continuity)} \\ &\leq \gamma \|u - \mathcal{I}^p u\|_{H^1(\Omega)} \|e\|_{H^1(\Omega)} \end{aligned} \quad (27)$$

Further invoking the interpolation error estimate of (15), together with the inequality of (27), we have [67]:

$$\|e\|_{H^1(\Omega)} \leq C_{1p} s^k \|u\|_{H^{k+1}(\Omega)}, \quad k = \min\{p, m\} \quad (28)$$

in which C_{1p} is a constant related to α, γ , and it is independent on s . Nonetheless, it is noted this error estimate does not consider the effect of numerical integration that turns out to be critical for Galerkin meshfree formulation.

3. Numerical integration and loss of Galerkin orthogonality

For Galerkin formulation, the domain integrations in Eqs. (24) and (25) have to be performed by certain quadrature rules. Here we describe two exemplar integration schemes, i.e., the conventional Gauss integration [10] and the recent reproducing kernel gradient smoothing integration [63].

3.1. Gauss integration scheme

For the conventional Gauss integration (GI) for Galerkin meshfree formulation, as shown in Fig. 1, we take 2D case as an example, where the problem domain is partitioned into a group of triangular integration cells, Ω_K 's, i.e., $\Omega = \{\Omega_K\}_{K=1}^{n_c}$, n_c is the total number of integration cells. The meshfree nodes usually also serve as the vertices of integration cells and the integration cell Ω_K can be conveniently measured by the characterized support size s . The Gauss quadrature rules are then invoked in each integration cell as indicated in Fig. 1, where an example is given for GI-3 that implies the 3-point Gauss integration rule.

For clarity, the Gauss integrations of the first and second integrals in Eq. (24) are listed as follows:

$$\begin{aligned} \int_{\Omega} \nabla \Psi_I \cdot \nabla \Psi_J d\Omega &\approx \int_{\Omega}^* \nabla \Psi_I \cdot \nabla \Psi_J d\Omega \\ &= \sum_{K=1}^{n_c} \int_{\Omega_K}^* \nabla \Psi_I \cdot \nabla \Psi_J d\Omega \\ &= \sum_{K=1}^{n_c} \sum_{G=1}^{n_g} \nabla \Psi_I(\mathbf{x}_G) \cdot \nabla \Psi_J(\mathbf{x}_G) J(\mathbf{x}_G) \omega_G \end{aligned} \quad (29)$$

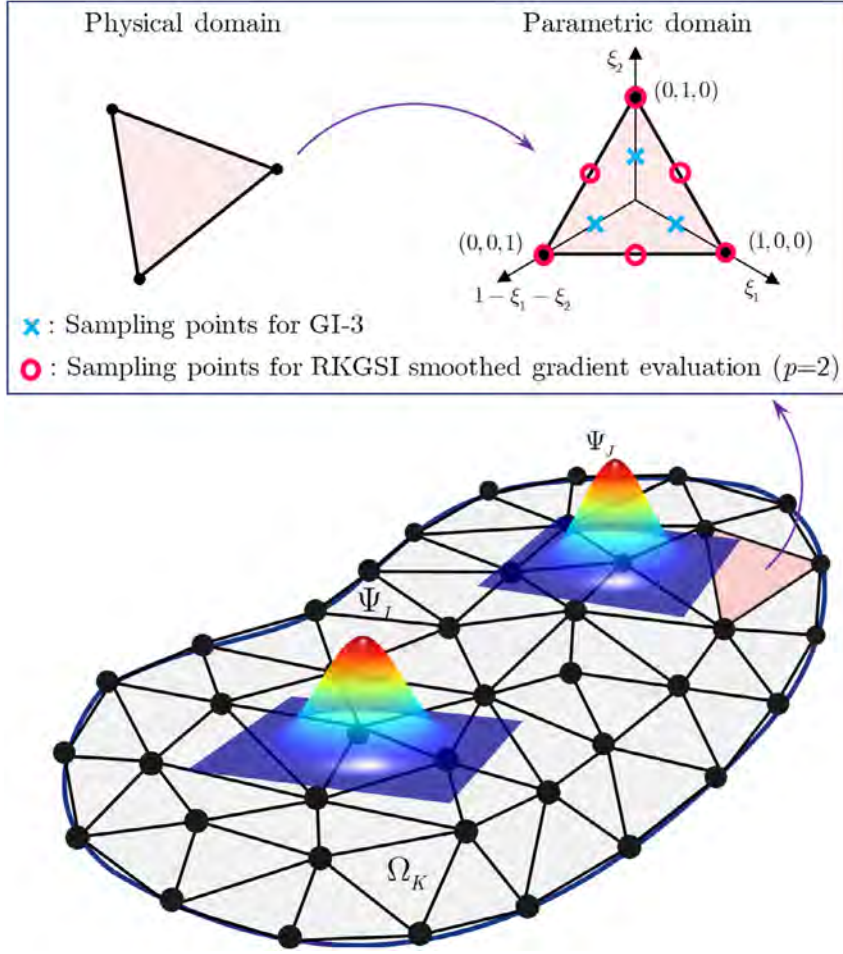


Fig. 1. Illustration of meshfree integration cells.

$$\begin{aligned}
 \int_{\partial\Omega} \Psi_I(\mathbf{n} \cdot \nabla \Psi_J) d\Gamma &\approx \int_{\partial\Omega}^* \Psi_I(\mathbf{n} \cdot \nabla \Psi_J) d\Gamma \\
 &= \sum_{B=1}^{n_b} \int_{\partial\Omega_B}^* \Psi_I(\mathbf{n} \cdot \nabla \Psi_J) d\Gamma \\
 &= \sum_{B=1}^{n_b} \sum_{G=1}^{n_g^b} \Psi_I(\mathbf{x}_G^b) [\mathbf{n}(\mathbf{x}_G^b) \cdot \nabla \Psi_J(\mathbf{x}_G^b)] J^b(\mathbf{x}_G^b) \varpi_G^b
 \end{aligned} \tag{30}$$

where the superscript asterisk denotes the numerical integration operator. \mathbf{x}_G 's and ϖ_G 's are the locations and weights of quadrature rules. J stands for the Jacobian that relates the physical and integration domains, n_g is the number of integration sampling points per integration cell. n_b is the number of the boundary integration segments $\partial\Omega_B$'s. \mathbf{x}_G^b , ϖ_G^b , J^b are the corresponding sampling points, weights and Jacobian for the boundary integration.

3.2. Integration consistency and reproducing kernel gradient smoothing integration

The integration consistency or integration constraint [40,57,60,63] represents the condition required by the Galerkin discrete formulation to exactly reproduce any solution spanned by the basis vector. Accordingly, for a

variable $u^h \in \mathcal{P}^q$, $\mathcal{P}^q = \text{span}\{\varphi_{ijk}\}_{i+j+k=0}^q$, $q \leq p$, suppose that all prescribed variables in Eq. (16) are evaluated by u^h , i.e. $g = u^h$, $b = -\Delta u^h$, the q th order integration consistency or integration constraint reads [63]:

$$\mathcal{A}^*(v^h, u^h) = \mathcal{B}^*(v^h, u^h), \forall v^h \in V^h, \forall u^h \in \mathcal{P}^q \quad (31)$$

with

$$\mathcal{A}^*(v^h, u^h) = \int_{\Omega}^* \nabla v^h \cdot \nabla u^h d\Omega - \int_{\partial\Omega}^* (\mathbf{n} \cdot \nabla v^h) u^h d\Gamma - \int_{\partial\Omega}^* v^h (\mathbf{n} \cdot \nabla u^h) d\Gamma + \beta \int_{\partial\Omega}^* v^h u^h d\Gamma \quad (32)$$

$$\mathcal{B}^*(v^h, u^h) = - \int_{\Omega}^* v^h \Delta u^h d\Omega - \int_{\partial\Omega}^* (\mathbf{n} \cdot \nabla v^h) u^h d\Gamma + \beta \int_{\partial\Omega}^* v^h u^h d\Gamma \quad (33)$$

where again \mathcal{A}^* and \mathcal{B}^* denote the corresponding operators after introducing numerical integration. In this circumstance, it is obviously that $\mathcal{B}(v^h, u^h) = \mathcal{F}(v^h)$. From Eq. (31), we can extract the following explicit expression for the q th order integration consistency condition [60,63]:

$$\int_{\Omega}^* \nabla v^h \cdot \nabla u^h d\Omega = \int_{\partial\Omega}^* v^h (\mathbf{n} \cdot \nabla u^h) d\Gamma - \int_{\Omega}^* v^h \Delta u^h d\Omega, \quad \forall v^h \in V^h, \forall u^h \in \mathcal{P}^q \quad (34)$$

Since the last two boundary terms in Eqs. (32) and (33) are identical when the numerical solution is an exact expansion of the q th order basis functions, thus they are dropped in Eq. (34). A numerical integration algorithm is said to meet the q th order integration consistency if the corresponding discrete Galerkin meshfree formulation satisfies Eq. (34). Now it has been well understood that the Galerkin meshfree formulation using Gauss quadrature rules does not fulfill the above integration consistency condition [40,60,63].

As mentioned earlier, several approaches have been proposed to construct consistent integration algorithms [40,57,60,62,63]. Among them, the reproducing kernel gradient smoothing integration method (RKGSI) [63] provides a convenient and general framework to develop arbitrary order explicit and consistent integration schemes. It is noted that RKGSI will reduce to SCNI when linear basis function is used in meshfree approximation [63]. Within this framework, the smoothed meshfree gradient $\tilde{\Psi}_{I,i}$ in a generic integration cell Ω_K , for example, the triangular cell in Fig. 1, takes the following reproducing kernel form [63]:

$$\tilde{\Psi}_{I,i}(\mathbf{x}) = \mathbf{q}^T(\mathbf{x}) \mathbf{G}^{-1} \mathbf{g}_{iI}, \quad \mathbf{x} \in \Omega_K \quad (35)$$

with

$$\mathbf{G} = \int_{\Omega_K}^* \mathbf{q}(\mathbf{x}) \mathbf{q}^T(\mathbf{x}) d\Omega \quad (36)$$

$$\mathbf{g}_{iI} = \int_{\partial\Omega_K}^* \Psi_I(\mathbf{x}) \mathbf{q}(\mathbf{x}) n_i d\Gamma - \int_{\Omega_K}^* \Psi_I(\mathbf{x}) \mathbf{q}_{,i}(\mathbf{x}) d\Omega \quad (37)$$

where $\mathbf{q} \in \mathcal{P}^{p-1}$ is the gradient basis vector that is one order lower than the original basis vector \mathbf{p} . In fact, provided that \mathbf{G} employs the same quadrature rules as those for the domain integration in \mathbf{K} , and \mathbf{g}_{iI} and \mathbf{f} also use identical quadrature rules, RKGSI will identically meet the p th order integration consistency regardless of numerical integration schemes. This inherent property of RKGSI can be clearly illustrated as follows.

For arbitrary variables $u \in \mathcal{P}^{p-1}$ and $v^h \in V^h$, they can be expressed as:

$$u_{,i}^h(\mathbf{x}) = \mathbf{a}_i^T \mathbf{q}(\mathbf{x}) \quad (38)$$

$$v^h(\mathbf{x}) = \sum_{I=1}^{n_p} \Psi_I(\mathbf{x}) w_I, \quad v_{,i}^h(\mathbf{x}) = \sum_{I=1}^{n_p} \tilde{\Psi}_{I,i}(\mathbf{x}) w_I \quad (39)$$

where \mathbf{a}_i is a constant coefficient vector and w_I is a nodal weight coefficient. Substituting Eqs. (38) and (39) into the left hand side of Eq. (34), together with Eqs. (35)–(37), we have:

$$\begin{aligned}
 \int_{\Omega}^* \nabla v^h \cdot \nabla u^h d\Omega &= \int_{\Omega}^* v_{,i}^h u_{,i}^h d\Omega = \sum_{K=1}^{n_c} \int_{\Omega_K}^* v_{,i}^h u_{,i}^h d\Omega \\
 &= \sum_{K=1}^{n_c} \sum_{I=1}^{n_p} w_I \mathbf{a}_i^T \int_{\Omega_K}^* \tilde{\Psi}_{I,i}(\mathbf{x}) \mathbf{q}(\mathbf{x}) d\Omega \\
 &= \sum_{K=1}^{n_c} \sum_{I=1}^{n_p} w_I \mathbf{a}_i^T \underbrace{\int_{\Omega_K}^* \mathbf{q}(\mathbf{x}) \mathbf{q}^T(\mathbf{x}) d\Omega}_{=\mathbf{G}} \mathbf{g}_{iI} \\
 &= \sum_{K=1}^{n_c} \left(\int_{\partial\Omega_K}^* \underbrace{\Psi_I(\mathbf{x}) w_I \mathbf{a}_i^T \mathbf{q}(\mathbf{x}) n_i}_{=u_{,i}^h} d\Gamma - \int_{\Omega_K}^* \underbrace{\Psi_I(\mathbf{x}) w_I \mathbf{a}_i^T \mathbf{q}_{,i}(\mathbf{x})}_{=u_{,ii}^h} d\Omega \right) \\
 &= \sum_{K=1}^{n_c} \left(\int_{\partial\Omega_K}^* v^h u_{,i}^h n_i d\Gamma - \int_{\Omega_K}^* v^h u_{,ii}^h d\Omega \right) \\
 &= \sum_{B=1}^{n_b} \int_{\partial\Omega_B}^* v^h (\mathbf{n} \cdot \nabla u^h) d\Gamma - \sum_{K=1}^{n_c} \int_{\Omega_K}^* v^h \Delta u^h d\Omega \\
 &= \int_{\partial\Omega}^* v^h (\mathbf{n} \cdot \nabla u^h) d\Gamma - \int_{\Omega}^* v^h \Delta u^h d\Omega
 \end{aligned} \tag{40}$$

Therefore, the integration consistency of Eq. (34) is ensured by the proposed RKGSi for any integration algorithm. As a result, the normal Gauss quadrature rules used in finite element analysis can be employed for the domain integration in the stiffness matrix \mathbf{K} :

$$\sum_{K=1}^{n_c} \int_{\Omega_K}^* \tilde{\Psi}_{I,i} \tilde{\Psi}_{J,i} d\Omega = \sum_{K=1}^{n_c} \sum_{G=1}^{n_g} \tilde{\Psi}_{I,i}(\mathbf{x}_G) \tilde{\Psi}_{J,i}(\mathbf{x}_G) J_K(\mathbf{x}_G) w_G \tag{41}$$

The computation of the reproducing kernel smoothed gradient $\tilde{\Psi}_{I,i}$ in Eq. (41) involves the evaluation of the vector \mathbf{g}_{iI} given by Eq. (37). It has been shown that based upon the gradient reproducing conditions stated in Eq. (12), a set of explicit quadrature rules for the domain and boundary integrations required by \mathbf{g}_{iI} , have been developed in [63] with particular reference to 2D triangular and 3D tetrahedral integration cells, where the total number of integration sampling points is minimized from a global point of view. Fig. 1 lists the integration sampling points for the RKGSi smoothed gradient computation with quadratic basis functions, more details on the RKGSi quadrature rules for cubic and 3D cases can be found in [63]. It is noted that these integration rules are also used for the force vector calculation in order to maintain the integration consistency of Galerkin meshfree formulation.

3.3. Loss of Galerkin orthogonality

Due to the fact that meshfree shape functions usually are not polynomials, numerical integration will inevitably introduce additional error for the discrete Galerkin meshfree formulation. Taking into account the numerical integration, the variational problem of Eq. (22) then becomes:

$$\text{Find } \tilde{u}^h \in V^h: \quad \mathcal{A}^*(v^h, \tilde{u}^h) = \mathcal{F}^*(v^h), \forall v^h \in V^h \tag{42}$$

in which \mathcal{A}^* and \mathcal{F}^* are the discrete counterparts of \mathcal{A} and \mathcal{F} after introducing numerical integration, and \tilde{u}^h is the corresponding numerical solution of the discrete Galerkin meshfree formulation with numerical integration.

Let $\tilde{\epsilon}$ be the real error between the exact solution u and the final solution \tilde{u}^h by solving the discrete meshfree equation obtained through numerical integration:

$$\tilde{\epsilon} = u - \tilde{u}^h \tag{43}$$

then the orthogonality condition of Eq. (26) for the continuous Galerkin weak form generally cannot be persevered for \tilde{e} :

$$\mathcal{A}(v^h, \tilde{e}) \neq 0, \quad \forall v^h \in V^h \quad (44)$$

Eq. (44) states that after we count the effect of numerical integration, the Galerkin orthogonality property is lost in the discrete meshfree formulation. Consequently, the solution error \tilde{e} cannot be easily estimated following the similar path described by the inequalities of (27) and (28). Instead, we would like to seek a bound for the error in the Galerkin orthogonality condition through incorporating the influence of numerical integration.

4. Accuracy of meshfree formulation incorporating integration error

In order to develop the error estimates for Galerkin meshfree methods incorporating the numerical integration effect, we first introduce the following theorem to evaluate the error arising from the loss of Galerkin orthogonality condition caused by the numerical integration.

4.1. Error estimate for Galerkin orthogonality

Theorem. For a regular solution $u \in C^m(\Omega)$, if the numerical integration scheme meets the q th order integration consistency condition, and a $(k-1)$ th order of accuracy is ensured for the domain integrations in Eq. (34), the orthogonality error regarding \tilde{e} defined by Eq. (43) is bounded as follows:

$$|\mathcal{A}(v^h, \tilde{e})| \leq C_\sigma s^k \|v^h\|_{H^1} |u|_{H^{k+1}} \quad \forall v^h \in V^h, \quad k = \min\{q, m\} \quad (45)$$

where C_σ is a constant related to the accuracy of numerical integration scheme used in Galerkin weak form.

Proof. Assume $\mathcal{T}^q u$ be a q th order Lagrange interpolant of $u \in C^m(\Omega)$ based upon the integration cells of Ω_K 's, following the standard procedure in the finite element error analysis, the corresponding interpolation error is measured by [75]:

$$\|u - \mathcal{T}^q u\|_{H^1} \leq C s^{k-l+1} |u|_{H^{k+1}}, \quad \forall l \leq k+1, \quad k = \min\{q, m\} \quad (46)$$

Since $\mathcal{T}^q u \in \mathcal{P}^q$ and the numerical integration scheme satisfies integration consistency condition, from Eq. (31), we have:

$$\mathcal{A}^*(v^h, \mathcal{T}^q u) = \mathcal{B}^*(v^h, \mathcal{T}^q u) \quad (47)$$

Subsequently, by combining Eqs. (42) and (47), the orthogonality expression for \tilde{e} can be recast as:

$$\begin{aligned} |\mathcal{A}(v^h, \tilde{e})| &= |(\mathcal{A} - \mathcal{A}^*)(v^h, \tilde{e}) + \mathcal{A}^*(v^h, \tilde{e})| \\ &= |(\mathcal{A} - \mathcal{A}^*)(v^h, \tilde{e}) + \mathcal{A}^*(v^h, u) - \mathcal{A}^*(v^h, \tilde{u}^h)| \\ &= |(\mathcal{A} - \mathcal{A}^*)(v^h, \tilde{e}) + \mathcal{A}^*(v^h, u) - \mathcal{B}^*(v^h, u)| \\ &= |(\mathcal{A} - \mathcal{A}^*)(v^h, \tilde{e}) + \mathcal{A}^*(v^h, u) - \mathcal{A}^*(v^h, \mathcal{T}^q u) - \mathcal{B}^*(v^h, u) + \mathcal{B}^*(v^h, \mathcal{T}^q u)| \\ &= |(\mathcal{A} - \mathcal{A}^*)(v^h, \tilde{e}) + \mathcal{A}^*(v^h, u - \mathcal{T}^q u) - \mathcal{B}^*(v^h, u - \mathcal{T}^q u)| \\ &= \left| (\mathcal{A} - \mathcal{A}^*)(v^h, \tilde{e}) + \mathcal{A}^*(v^h, u - \mathcal{T}^q u) - \mathcal{B}^*(v^h, u - \mathcal{T}^q u) \right. \\ &\quad \left. - \mathcal{A}(v^h, u - \mathcal{T}^q u) + \mathcal{A}(v^h, u - \mathcal{T}^q u) + \mathcal{B}(v^h, u - \mathcal{T}^q u) - \mathcal{B}(v^h, u - \mathcal{T}^q u) \right| \\ &= \left| (\mathcal{A} - \mathcal{A}^*)(v^h, \tilde{e}) - (\mathcal{A} - \mathcal{A}^*)(v^h, u - \mathcal{T}^q u) \right. \\ &\quad \left. + (\mathcal{B} - \mathcal{B}^*)(v^h, u - \mathcal{T}^q u) + (\mathcal{A} - \mathcal{B})(v^h, u - \mathcal{T}^q u) \right| \end{aligned} \quad (48)$$

Meanwhile, since both u and $\mathcal{T}^q u$ are regular solutions, the following relationships hold:

$$\mathcal{A}(v^h, u) = \mathcal{B}(v^h, u) \quad (49)$$

$$\mathcal{A}(v^h, \mathcal{T}^q u) = \mathcal{B}(v^h, \mathcal{T}^q u) \quad (50)$$

Subtracting Eq. (50) from (49) then yields:

$$(\mathcal{A} - \mathcal{B})(v^h, u - \mathcal{T}^q u) = 0 \quad (51)$$

Consequently, further invoking the triangle inequality on Eq. (48) leads to:

$$\begin{aligned} |\mathcal{A}(v^h, \tilde{e})| &\leq |(\mathcal{A} - \mathcal{A}^*)(v^h, \tilde{e})| \\ &\quad + |(\mathcal{A} - \mathcal{A}^*)(v^h, u - \mathcal{T}^q u)| \\ &\quad + |(\mathcal{B} - \mathcal{B}^*)(v^h, u - \mathcal{T}^q u)| \end{aligned} \quad (52)$$

Eq. (52) implies that the error in the Galerkin orthogonality condition is bounded by the various parts of numerical integration errors. Regarding the numerical integration operations, it has been shown that for two sufficiently smooth functions v and u , with the help of Schwarz inequality and Eq. (46), the numerical integration error for an inner product satisfies the following bound [66,76,77]:

$$\begin{aligned} |(v, u - \mathcal{T}^q u) - (v, u - \mathcal{T}^q u)^*| &\leq \sigma |(v, u - \mathcal{T}^q u)| \\ &\leq C_\sigma \|v\|_{H^l} \|u - \mathcal{T}^q u\|_{H^l} \\ &\leq C_\sigma s^{k-l+1} \|v\|_{H^l} |u|_{H^{k+1}} \end{aligned} \quad (53)$$

in which $(\cdot, \cdot): H^l \times H^l \rightarrow \mathbb{R}^{n_{sd}}$ defines an arbitrary inner product in Ω , σ is a constant related to numerical integration scheme [76]. The validity of the inequality (53) is ensured if the employed numerical integration scheme for the inner product is $(k-l)$ th order accurate.

For illustration purpose, we specifically consider two typical error estimates in the inequality of (52), one for domain integration and the other one for boundary integration:

$$\left| \int_{\Omega} v_{,i}^h (u - \mathcal{T}^q u)_{,i} d\Omega - \int_{\Omega}^* v_{,i}^h (u - \mathcal{T}^q u)_{,i} d\Omega \right| \leq C_\sigma s^k \|v^h\|_{H^1} |u|_{H^{k+1}} \quad (54)$$

$$\begin{aligned} \left| \int_{\partial\Omega} v^h (u - \mathcal{T}^q u)_{,i} n_i d\Gamma - \int_{\partial\Omega}^* v^h (u - \mathcal{T}^q u)_{,i} n_i d\Gamma \right| &\leq C_\sigma \sum_{K=1}^{n_c} |v^h|_{H^{1/2}(\partial\Omega)} |u - \mathcal{T}^q u|_{H^{1/2}(\partial\Omega)} \\ &\leq C_\sigma \sum_{K=1}^{n_c} \|v^h\|_{H^1} \|u - \mathcal{T}^q u\|_{H^1} \\ &\leq C_\sigma s^k \|v^h\|_{H^1} |u|_{H^{k+1}} \end{aligned} \quad (55)$$

where the Sobolev trace theorem [75] is used to derive the relationship of (55) and once again it is noted that the accuracy order for domain and boundary integrations should be at least $(k-1)$. As a result, all terms in (52) are bounded as follows:

$$|(\mathcal{A} - \mathcal{A}^*)(v^h, \tilde{e})| \leq C_\sigma |\mathcal{A}(v^h, \tilde{e})| \quad (56)$$

$$|(\mathcal{A} - \mathcal{A}^*)(v^h, u - \mathcal{T}^q u)| \leq C_\sigma s^k \|v^h\|_{H^1} |u|_{H^{k+1}} \quad (57)$$

$$|(\mathcal{B} - \mathcal{B}^*)(v^h, u - \mathcal{T}^q u)| \leq C_\sigma s^k \|v^h\|_{H^1} |u|_{H^{k+1}} \quad (58)$$

in which $k = \min\{q, m\}$. A combination of (56)–(58) and (52) immediately leads to the desired result of (45). This completes the proof of the orthogonality error estimate for Galerkin meshfree formulation.

4.2. H^1 and L^2 error estimates

With the aid of triangle inequality [74], the error of \tilde{e} can be conveniently partitioned into two parts:

$$\begin{aligned} \|\tilde{e}\| &= \|u - \tilde{u}^h\| \\ &= \|u - u^h + u^h - \tilde{u}^h\| \\ &\leq \|u - u^h\| + \|u^h - \tilde{u}^h\| \\ &= \|e\| + \|\eta\| \end{aligned} \quad (59)$$

where $\eta = u^h - \tilde{u}^h$. The first term of Eq. (59) is already given in Eq. (28). Based upon the coercivity of \mathcal{A} defined by (20) and the orthogonality error estimate illustrated by (45), the H^1 error of $\eta = u^h - \tilde{u}^h$ can be attained as follows:

$$\alpha \|\eta\|_{H^1}^2 \leq |\mathcal{A}(\eta, \eta)| = |\mathcal{A}(\eta, \tilde{e})| \leq C_\sigma s^l \|\eta\|_{H^1} |u|_{H^{l+1}} \quad (60)$$

or

$$\|\eta\|_{H^1} \leq C_{1q} s^l |u|_{H^{l+1}}, \quad l = \min\{q, m\} \quad (61)$$

where C_{1q} is a constant related to α, σ and we have used the relationships of $\tilde{e} = e + \eta$ and $\mathcal{A}(\eta, e) = 0$. Substituting (28) and (61) into Eq. (59) then gives the H^1 error estimate for \tilde{e} :

$$\|\tilde{e}\|_{H^1} \leq C_{1p} s^k |u|_{H^{k+1}} + C_{1q} s^l |u|_{H^{l+1}}, \quad k = \min\{p, m\}, \quad l = \min\{q, m\} \quad (62)$$

In order to obtain the L^2 error estimate for \tilde{e} , in light of the classical Aubin–Nitsche trick [74], we consider the auxiliary dual problem:

$$\text{Find } w \in H^1(\Omega): \quad \mathcal{A}(v, w) = \mathcal{F}(v), \quad \forall v \in H^1(\Omega) \quad (63)$$

which corresponds to the following strong form:

$$\begin{cases} -w_{,ii} = \tilde{e}, & \text{in } \Omega \\ w = 0, & \text{on } \partial\Omega \end{cases} \quad (64)$$

where the homogeneous boundary condition is assumed without loss of generality.

Meanwhile, according to the closed graph theorem [74], the following relationship holds:

$$|w|_{H^2} \leq C \|\tilde{e}\|_{L^2} \quad (65)$$

Subsequently, by choosing the \tilde{e} as the test function in Eq. (63), the L^2 error for \tilde{e} can be expressed as:

$$\begin{aligned} \|\tilde{e}\|_{L^2}^2 &= |\mathcal{F}(\tilde{e})| = |\mathcal{A}(\tilde{e}, w)| \\ &= \left| \mathcal{A}(\tilde{e}, w - \mathcal{T}^1 w) - \underbrace{\mathcal{A}(\tilde{e}, \mathcal{T}^1 w)}_{=0} \right| \\ &= |\mathcal{A}(\tilde{e}, w - \mathcal{T}^1 w)| \\ &\leq \gamma \|w - \mathcal{T}^1 w\|_{H^1} \|\tilde{e}\|_{H^1} \end{aligned} \quad (66)$$

in which $\mathcal{T}^1 w \in \mathcal{P}^1$ is an interpolation of w with linear basis meshfree shape functions, thus $\mathcal{T}^1 w = 0$ on $\partial\Omega$ and $(\mathcal{T}^1 w)_{,ii} = 0$, which leads to:

$$\mathcal{A}(\mathcal{T}^1 w, \tilde{e}) = \mathcal{B}(\tilde{e}, \mathcal{T}^1 w) = 0 \quad (67)$$

Following the interpolation error of (46) and the relationship of (65), we then have:

$$\|w - \mathcal{T}^1 w\|_{H^1} \leq Cs |w|_{H^2} \leq Cs \|\tilde{e}\|_{L^2} \quad (68)$$

Consequently, substituting (68) into (66) finally gives the following L^2 -error estimate:

$$\|\tilde{e}\|_{L^2} \leq C_\gamma s \|\tilde{e}\|_{H^1} \quad (69)$$

or

$$\|\tilde{e}\|_{L^2} \leq C_{0p} s^{k+1} |u|_{H^{k+1}} + C_{0q} s^{l+1} |u|_{H^{l+1}}, \quad k = \min\{p, m\}, \quad l = \min\{q, m\} \quad (70)$$

where C_{0p} is a constant related to α, γ , and C_{0q} is a constant related to α, γ, σ , respectively.

As shown by the inequalities of (62) and (70), unlike the standard error estimates for Galerkin finite element methods, both L^2 and H^1 errors for Galerkin meshfree methods actually contain two parts, one comes from the interpolation error of meshfree approximation space which is similar as the finite element error estimate, and the other one is attributed to the numerical integration of Galerkin weak form which usually does not occur in finite element formulation. More specifically, the meshfree reproducing conditions or approximation consistency controls the interpolation error, and the integration consistency governs the numerical integration error. Consequently, in order to ensure that the numerical integration error does not deteriorate the overall algorithmic convergence rate, we need $q = p$ which means that the numerical integration schemes should at least fulfill the p th order integration consistency condition to achieve the expected optimal convergence of Galerkin meshfree solutions.

Table 1

Theoretical ultimate convergence rates of Galerkin meshfree methods using different integration schemes.

Integration scheme	GI	RKGSi
Order of basis functions	p	p
Order of integration consistency	$q = 0$	$q = p$
Convergence rate of L^2 -error	1	$p + 1$
Convergence rate of H^1 -error	0	p

4.3. Assessment of integration consistency

In accordance with the error estimates of (62) and (70), the theoretical convergence rates for Galerkin meshfree formulations using Gauss integration (GI) and the reproducing kernel gradient smoothing integration (RKGSi) are presented in Table 1. In the subsequent discussions, GI particularly represents the Galerkin meshfree formulation with Gauss integration and standard gradients of meshfree shape functions. Because GI does not meet any order of integration consistency, we have $q = 0$ and the convergence rates referring to L^2 and H^1 errors for different Gauss quadrature rules will be ultimately limited to 1 and 0, regardless of the order of Gauss integration. On the contrary, RKGSi meets the p th order integration consistency condition, say, $q = p$, thus the optimal convergence rates of $(p + 1)$ and p with respect to L^2 and H^1 errors can be attained.

Moreover, for the convenience of subsequent development, several specific quadrature rules of GI and their accuracy orders are listed in Table 2 [78,79], where both quadratic and cubic basis functions are considered. The normal rules imply the full integration corresponding to the degree of basis functions, which are used in the finite element analysis for proper stiffness integration. Of course, since meshfree shape functions are not polynomials, the normal rules usually are not enough for the stiffness evaluation by GI, while they can serve a reasonable reference of low order rules for comparison purpose. In addition, the quadrature rules which employ more sampling points than the normal rules are denoted as high order rules. While, the normal rules are adequate for the stiffness computation by RKGSi through replacing the conventional gradients by the reproducing kernel smoothed gradients at Gauss points. It is also noted that a prerequisite for the relationship of (45) is that the quadrature rules should be $(q - 1)$ th order accurate. This condition can be easily satisfied by the quadrature rules in Table 2, since they are at least $(p - 1)$ th order accurate and we also have the fact of $q \leq p$. In the meantime, the explicit quadrature rules used for the computation of g_{iI} in RKGSi are $2(p - 1)$ th order accurate [63], thus the inequality of (45) holds for both GI with $q = 0$ and RKGSi with $q = p$.

To more clearly illustrate the integration consistency, the integration consistency conditions are examined for one- (1D) two- (2D) and three-dimensional (3D) quadratic and cubic meshfree formulations using various integration schemes, where GI- k implies that k Gauss quadrature points are used in each integration cell. The numerical tests are realized through verifying the relationship of Eq. (31) with $v^h = \Psi_I$ and $u^h = (\sum_{i=1}^{n_{sd}} x_i)^p$ for irregular meshfree discretizations. Figs. 2–6 present the integration consistency test results, where meshfree nodes are denoted by solid circles. These results obviously manifest that GI does not meet any order of the integration consistency condition, i.e. $q = 0$, even for very high order quadrature rules such as GI-9 for 1D, GI-16 for 2D and GI-20 for 3D meshfree formulations with cubic basis functions, respectively. By contrast, RKGSi exactly satisfies the p th order integration consistency condition, i.e., $q = p$.

5. Numerical results

In order to validate the proposed accuracy measures for Galerkin meshfree formulation, this Section presents a series of numerical examples which employ the consistent integration scheme (RKGSi) and the conventional non-consistent Gauss integration scheme (GI, k th order Gauss integration rule is denoted by GI- k). Both the normal and high order quadrature rules in Table 2 are considered to examine the influence of numerical integration on the overall accuracy of Galerkin meshfree methods. The relative L^2 and H^1 error norms are utilized for the accuracy comparison:

$$L^2\text{-error} = \frac{\|u - \tilde{u}^h\|_{L^2}}{\|u\|_{L^2}}, \quad H^1\text{-error} = \frac{\|u - \tilde{u}^h\|_{H^1}}{\|u\|_{H^1}} \quad (71)$$

Table 2
Number of integration points for GI.

Integration cell	Basis degree p	Number of GI sampling points (precision)	
		Normal rule	High order rule
1D Line segment	2	2 (3)	8 (15)
	3	3 (5)	9 (17)
2D Triangle	2	3 (2)	13 (7)
	3	6 (4)	16 (8)
3D Tetrahedron	2	4 (2)	14 (4)
	3	11 (4)	20 (5)

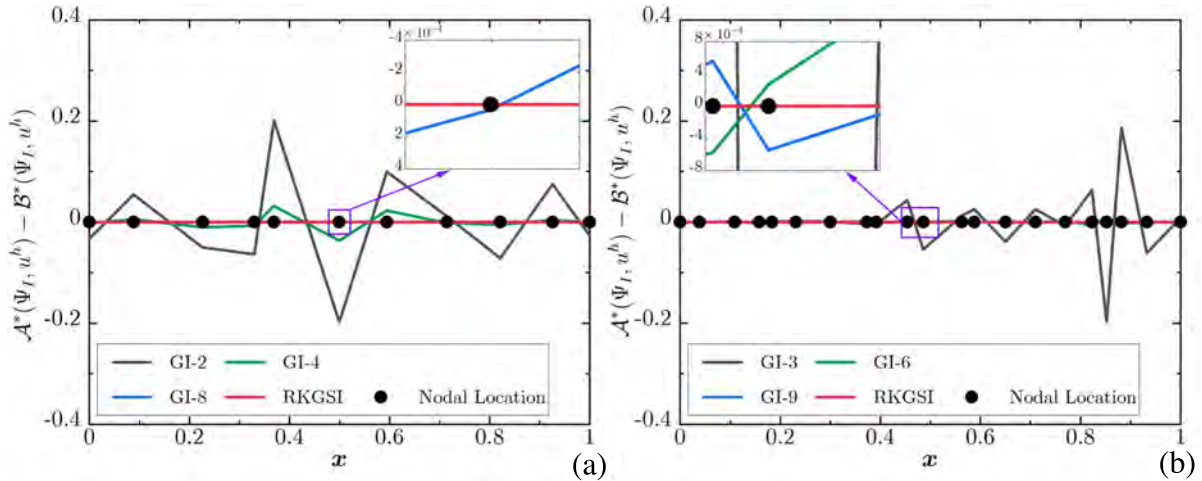


Fig. 2. Examination of the p th order integration consistency for 1D meshfree formulation: (a) $p = 2$; (b) $p = 3$.

where it is noted that \tilde{u}^h stands for the final Galerkin meshfree solution. Moreover, “CR” denotes the convergence rate throughout the subsequent numerical results, and thus theoretical CR and numerical CR imply the theoretical and numerical convergence rates, respectively.

5.1. 1D elastic rod

Consider the 1D rod problem fixed at the left end as shown in Fig. 7, the body force is $b(x) = -\sin(\pi x/(2L))$ with L being the rod length. The dimensionless geometric and material parameters for this problem are: length $L = 10$, cross section area $A = 1$, Young’s modulus $E = 1$. The analytical solution for this problem is given by:

$$u(x) = \sin\left(\frac{\pi x}{2L}\right) \quad (72)$$

For this problem, meshfree discretizations with 11, 21, 41, 81, 161, and 321 nodes are employed for the convergence study. The normalized support sizes of 2.5 and 3.5 are utilized for the quadratic and cubic meshfree formulations, respectively. Figs. 8–11 present the convergence results referring to the L^2 and H^1 error norms, where the horizontal axis “ s ” denotes the support size, and the dashed lines illustrate the numerical CR. It is evident that the Gauss integration rules, such as GI-2, GI-4 and GI-8 for quadratic formulation and GI-3, GI-6 and GI-9 for cubic formulation, could not produce the expected optimal convergence rates for L^2 and H^1 error norms, namely, 3 and 2 for the quadratic case and 4 and 3 for the cubic case, respectively. These observations can be explained by the inequalities of (62) and (70), where for the Gauss quadrature rules we have $p = 2$ and $q = 0$ for quadratic formulation and $p = 3$ and $q = 0$ for the cubic formulation. Consequently, following the inequalities of (62) and (70) as well as Table 1, it turns out that the solution errors of GI’s are dominated by the integration error rather than the interpolation error. Even very high order quadrature rule like GI-8 only enables the optimal

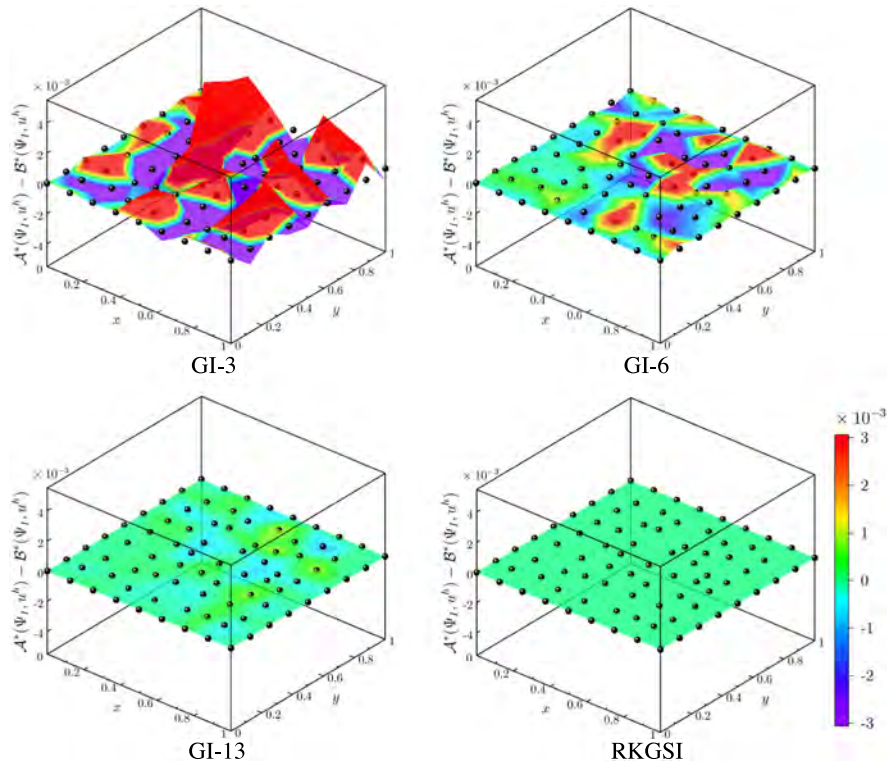


Fig. 3. Examination of the 2nd order integration consistency for 2D quadratic meshfree formulation.

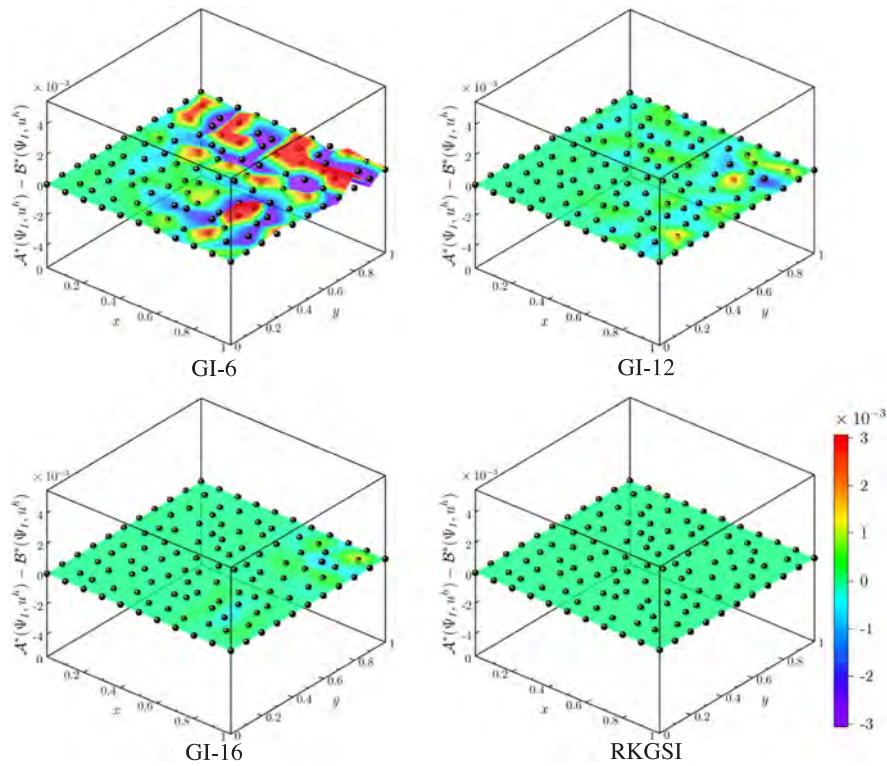


Fig. 4. Examination of the 3rd order integration consistency for 2D cubic meshfree formulation.

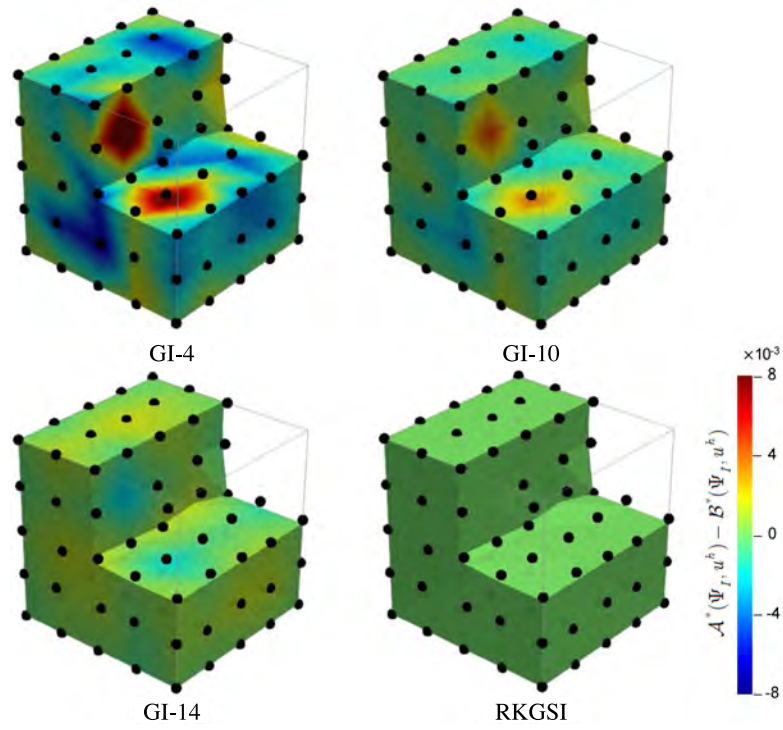


Fig. 5. Examination of the 2nd order integration consistency for 3D quadratic meshfree formulation.

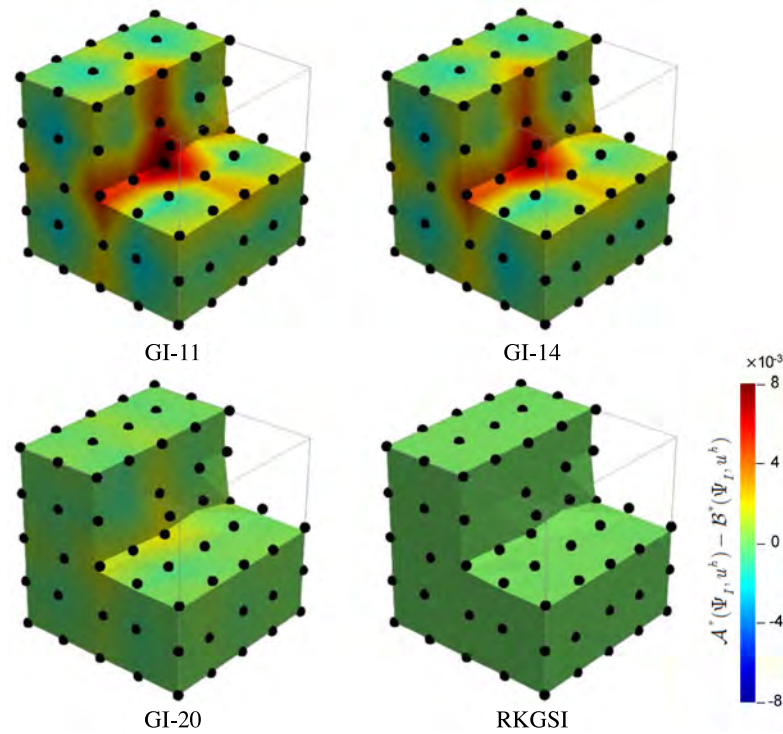


Fig. 6. Examination of the 3rd order integration consistency for 3D cubic meshfree formulation.

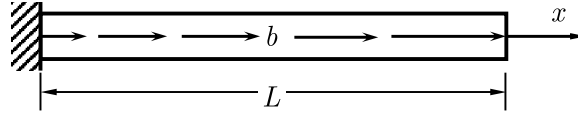
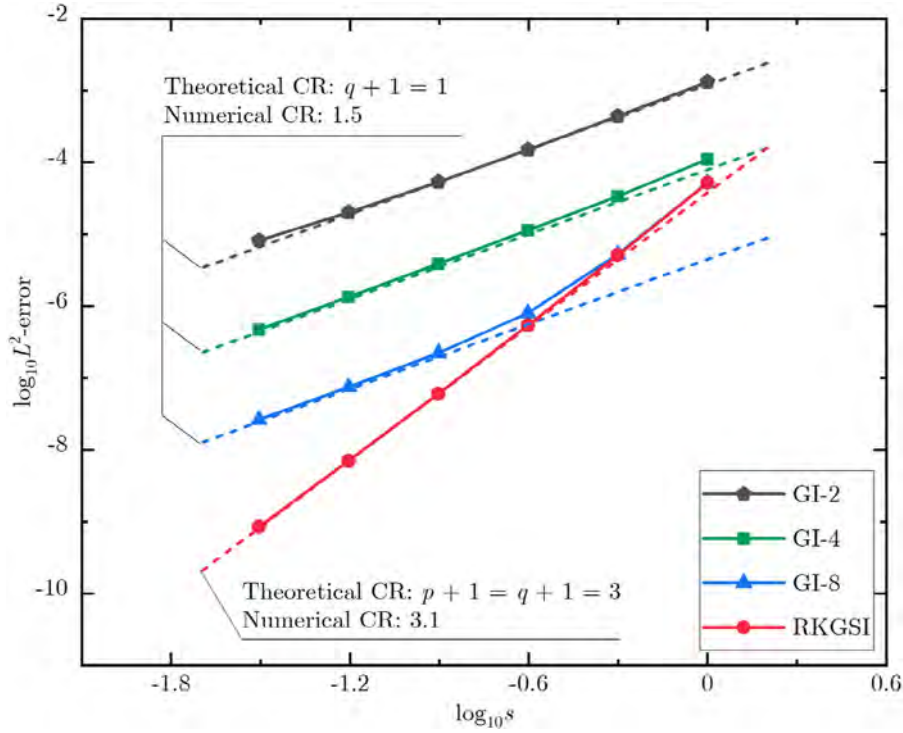


Fig. 7. Description of the 1D rod problem.

Fig. 8. L^2 -error convergence comparison for the 1D rod problem using quadratic meshfree formulation.

convergence of quadratic meshfree formulation for the initial coarse discretizations, where the interpolation error outplays the integration error for relatively larger nodal distance. However, when the discretizations are refined, the overall convergence of meshfree formulation is gradually governed by the integration error, i.e., for smaller nodal distance, the integration error becomes larger than the interpolation error. Therefore, the solutions computed by GI's are eventually controlled by the integration errors because these methods violate the integration consistency condition or integration constraint. The numerical results also evince that the ultimate convergence rates of GI's are slightly higher than $(q + 1)$ for L^2 -error and q for H^1 -error. This is perhaps due to the fact that the proposed theoretical development of error estimates relies on the conventional polynomial assumption and the meshfree shape functions actually are rational. This observation is also revealed by the interpolation error estimate of (28), i.e., the interpolation order is often slightly higher than the basis degree in practice [1–8]. On the other hand, in case of the quadratic and cubic meshfree formulations with RKGSI, we have $q = p = 2$ and $q = p = 3$ in the inequalities of (62) and (70). Thus, as shown in Figs. 8–11, optimal convergence results regarding both L^2 and H^1 error norms are achieved by RKGSI, which fully agree with the theoretical results in Table 1.

5.2. 2D square domain potential problem

As shown in Fig. 12, consider a 2D potential problem in a square domain with a length of $L = 1$, where the left and the bottom sides are Neumann boundaries, and the right and the top sides are essential boundaries. The prescribed boundary values and the source term of this problem is computed according to following manufactured

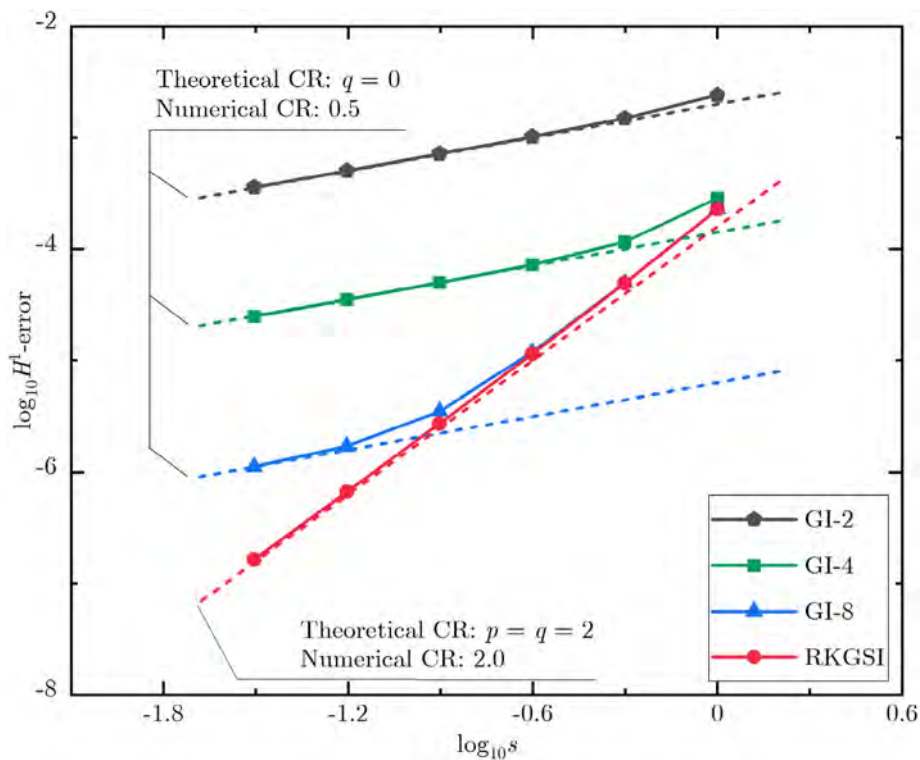


Fig. 9. H^1 -error convergence comparison for the 1D rod problem using quadratic meshfree formulation.

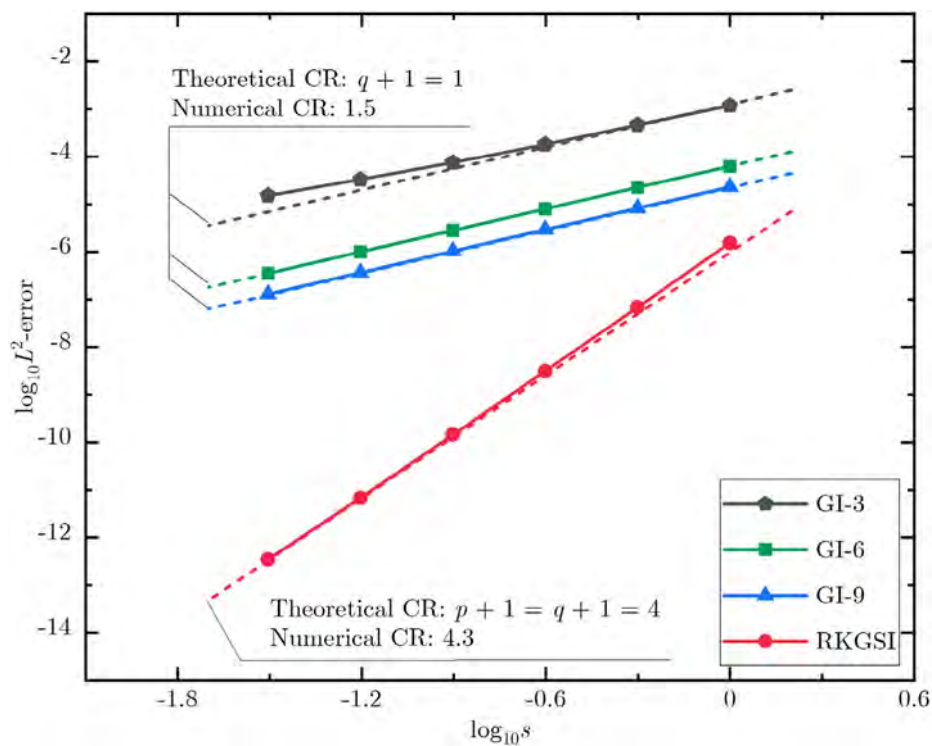


Fig. 10. L^2 -error convergence comparison for the 1D rod problem using cubic meshfree formulation.

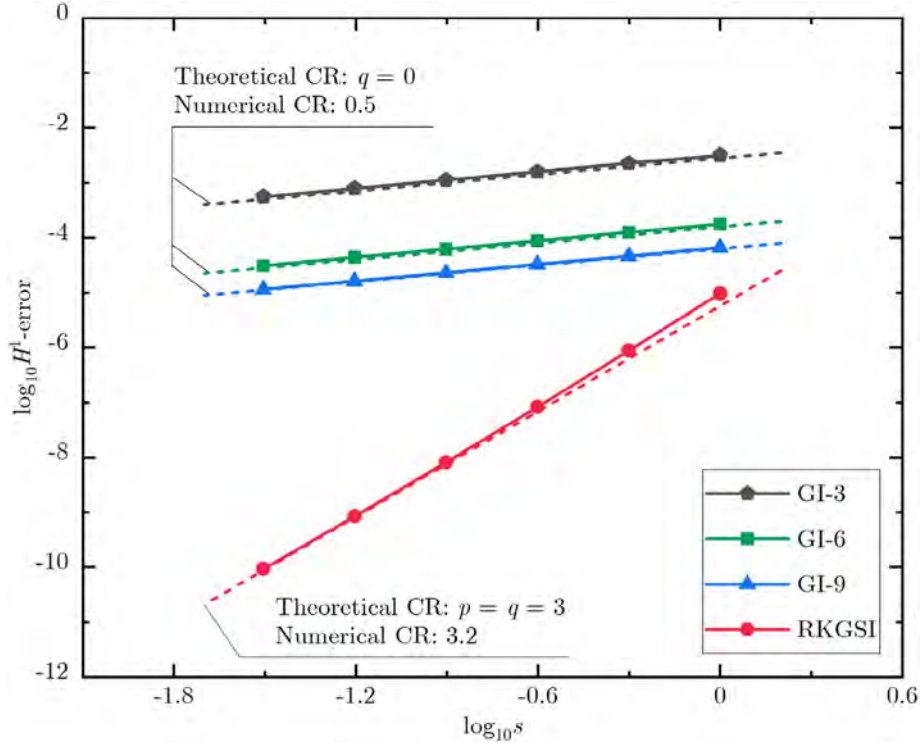


Fig. 11. H^1 -error convergence comparison for the 1D rod problem using cubic meshfree formulation.

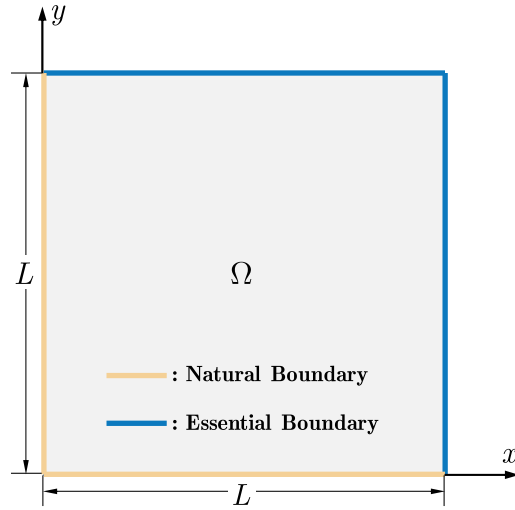


Fig. 12. Description of the 2D square domain potential problem.

exact solution:

$$u(\mathbf{x}) = \sin\left(\frac{\pi}{2L}x\right) \sin\left(\frac{\pi}{2L}y\right) \quad (73)$$

Six progressively refined meshfree discretizations with 6×6 , 11×11 , 21×21 , 41×41 , 81×81 and 161×161 nodes are employed for the convergence assessment of this problem, where the first three discretizations are listed in Fig. 13. In the quadratic and cubic meshfree methods, normalized support sizes of 2.5 and 3.5 are

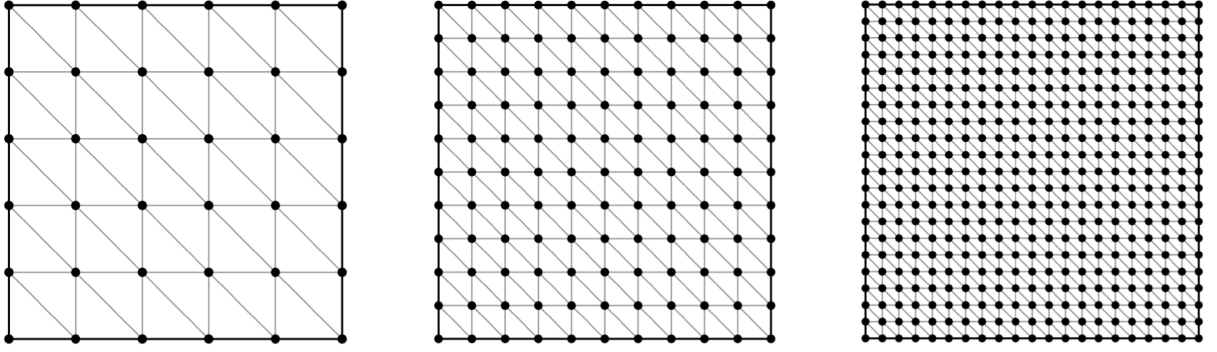


Fig. 13. Meshfree discretizations for the 2D square domain potential problem: 36, 121 and 441 nodes.

adopted for the kernel function. The convergence results of this 2D square domain potential problem are plotted in Figs. 14 and 15 for the quadratic meshfree formulation, and Figs. 16 and 17 for the cubic meshfree formulation, respectively. Similar to the previous 1D results, it is apparent from Figs. 14 and 15 that the results of GI-3 and GI-6 are completely governed by the integration errors, even GI-13 only produces better convergent results for very coarse discretizations, and this convergence is lost with refined discretizations. For the cubic case as listed in Figs. 16 and 17, all three GI methods including GI-6, GI-12 and GI-16 are not capable of achieving optimally convergent results. Figs. 16–17 also indicate that the convergence rates of all numerical results by GI's are approximately 1.5 for L^2 -error and 0.5 for H^1 -error, no matter what meshfree basis functions and GI quadrature rules are used. These results closely follow the theoretical predictions in Table 1, which gives 1 and 0 for the slopes of L^2 and H^1 errors because GI's do not meet the integration consistency and $q = 0$. As mentioned earlier, the small deviation between the theoretical and numerical convergence rates might attribute to the rational meshfree shape functions. Meanwhile, the numerical results of RKGSi in Figs. 14–17 unanimously support the optimal convergence rates of Galerkin meshfree methods listed in Table 1, namely, $(p + 1)$ and p with respect to L^2 and H^1 errors.

5.3. 2D elastic plate with a circular hole

As shown in Fig. 18, an infinite elastic plate with a circular hole is subjected to a x -direction far field load of $T = 1000$. Under the plane stress condition, the analytical solution for this problem [80] is:

$$\begin{cases} u_x = \frac{Ta}{8\mu} \left[\frac{r}{a}(\kappa + 1) \cos \theta + \frac{2a}{r}((1 + \kappa) \cos \theta + \cos 3\theta) - \frac{2a^3}{r^3} \cos 3\theta \right] \\ u_y = \frac{Ta}{8\mu} \left[\frac{r}{a}(\kappa - 3) \sin \theta + \frac{2a}{r}((1 - \kappa) \sin \theta + \sin 3\theta) - \frac{2a^3}{r^3} \sin 3\theta \right] \end{cases} \quad (74)$$

in which (r, θ) are the polar coordinates, $\mu = E/2/(1 + \nu)$, $\kappa = (3 - \nu)/(1 + \nu)$, E and ν are the Young's modulus and Poisson's ratio, respectively. During the computation, by taking the symmetry advantage, only a finite-size quarter model is analyzed, exact displacement and symmetric boundary conditions are enforced as shown in Fig. 18. The dimensionless geometric and material parameters are: length $L = 4$, hole radius $a = 1$, Young's modulus $E = 2 \times 10^7$, Poisson ratio $\nu = 0.3$.

For this elastic plate with a circular hole problem, non-uniform meshfree discretizations using 104, 362, 1373, 5345 and 21089 nodes are utilized for the convergence study, where the first three progressively refined discretizations are portrayed in Fig. 19. The quadratic basis function with a normalized support size of 2.1 is employed to construct meshfree shape functions. The convergence results are presented in Fig. 20 for the L^2 -error and in Fig. 21 for the H^1 -error, which again confirm that GI's lose the optimal convergence and this issue cannot be well remedied by just increasing the number of Gauss integration points. A direct comparison in Figs. 20 and 21 shows that optimal convergence rates of 3 and 2 are ensured by RKGSi for both L^2 and H^1 error norms.

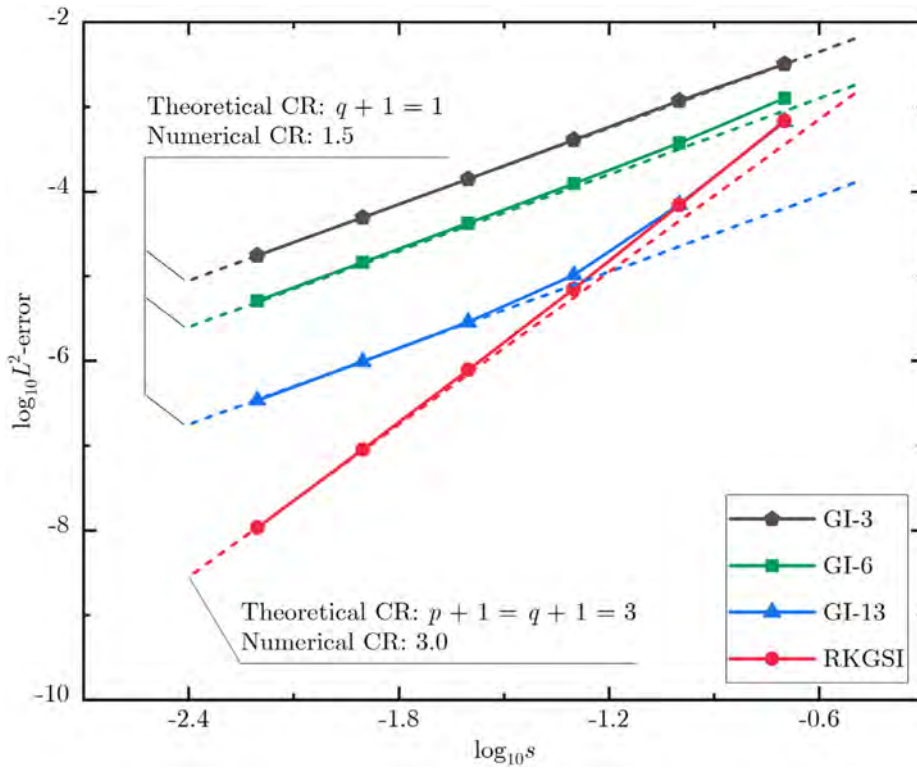


Fig. 14. L^2 -error convergence comparison for the 2D square domain potential problem using quadratic meshfree formulation.

5.4. 3D cubic domain potential problem

To further assess the proposed theoretical results, a 3D cubic domain potential problem as shown in Fig. 22 is investigated. This cube has a unit length for all three directions, and a manufactured solution of $u(\mathbf{x}) = \exp(x+y+z)$ is taken as the exact solution. On the boundary surfaces of $x = 0$, $y = 0$, $z = 0$, essential boundary conditions are applied and the natural boundary conditions are imposed on the rest of surfaces. All prescribed boundary values are evaluated in accordance with the exact solution. Meshfree discretizations of $5 \times 5 \times 5$, $7 \times 7 \times 7$, $9 \times 9 \times 9$, $13 \times 13 \times 13$, $17 \times 17 \times 17$, and $25 \times 25 \times 25$ nodes are adopted for the convergence analysis of Galerkin meshfree methods, where the first three node distributions are plotted in Fig. 23. The normalized support sizes are 2.1 and 3.1 for quadratic and cubic meshfree formulations. The convergence results for this 3D cubic domain potential problem are given in Figs. 24–27, which reveal that for both quadratic and cubic meshfree formulations, high order Gauss integration rules such as GI-14 and GI-20 exhibit the same convergence behaviors as the relatively lower order rules GI-4 and GI-11 for quadratic and cubic cases, since all of them fail to meet the integration consistency condition. In contrast to GI's, as demonstrated in Figs. 24–27, RKGSI has the inherent property of integration consistency and yields optimally convergent results for both L^2 and H^1 errors, which signifies the importance of integration consistency for Galerkin meshfree analysis.

5.5. 3D hollow cylinder potential problem

The last numerical example is a 3D hollow cylinder potential problem as described in Fig. 28. This hollow cylinder has a height of $L = 1$ and its inner and outer radii are $r_i = 1$ and $r_o = 2$. Due to the symmetry, a quarter hollow cylinder is modeled, where natural boundary conditions are applied at $x = 0$, $y = 0$, and the rest of surfaces are subjected to essential boundary conditions. The prescribed values of both essential and natural boundary

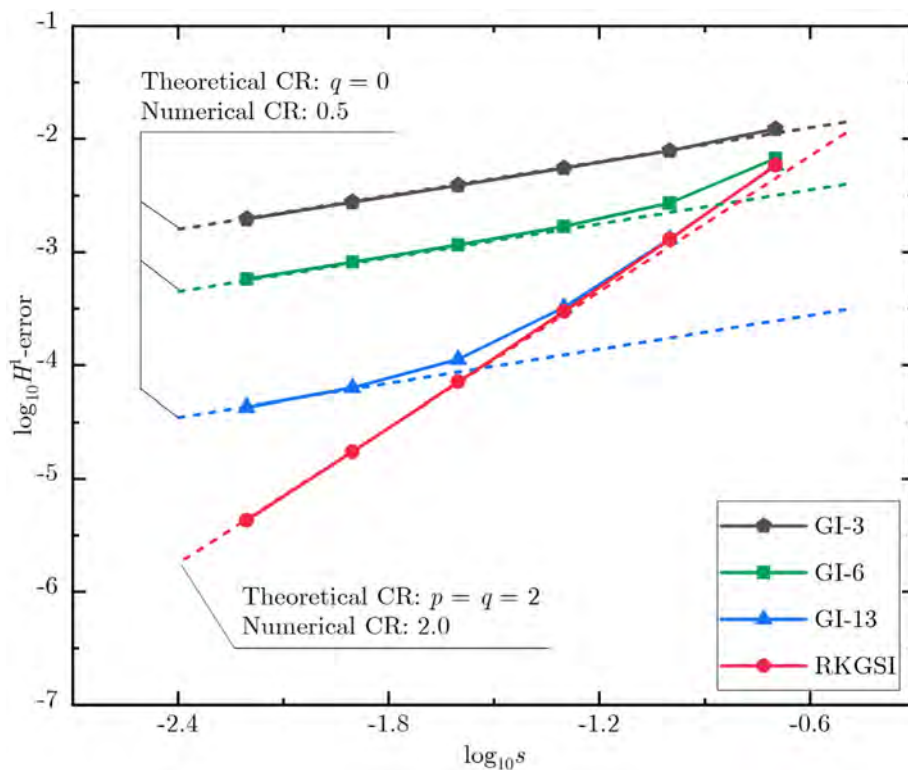


Fig. 15. H^1 -error convergence comparison for the 2D square domain potential problem using quadratic meshfree formulation.

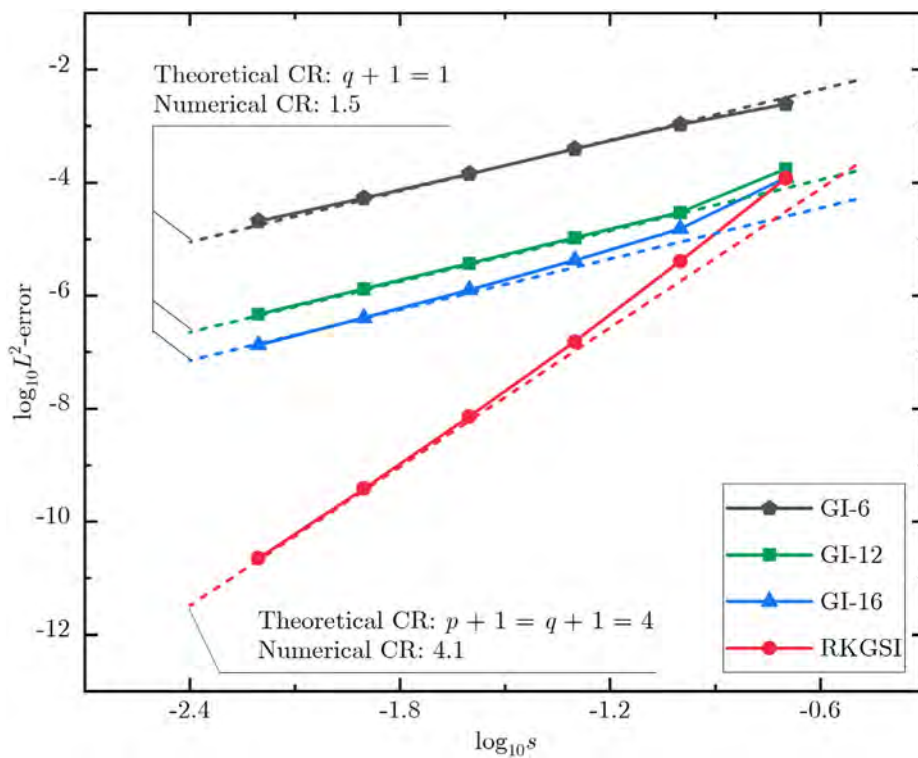


Fig. 16. L^2 -error convergence comparison for the 2D square domain potential problem using cubic meshfree formulation.

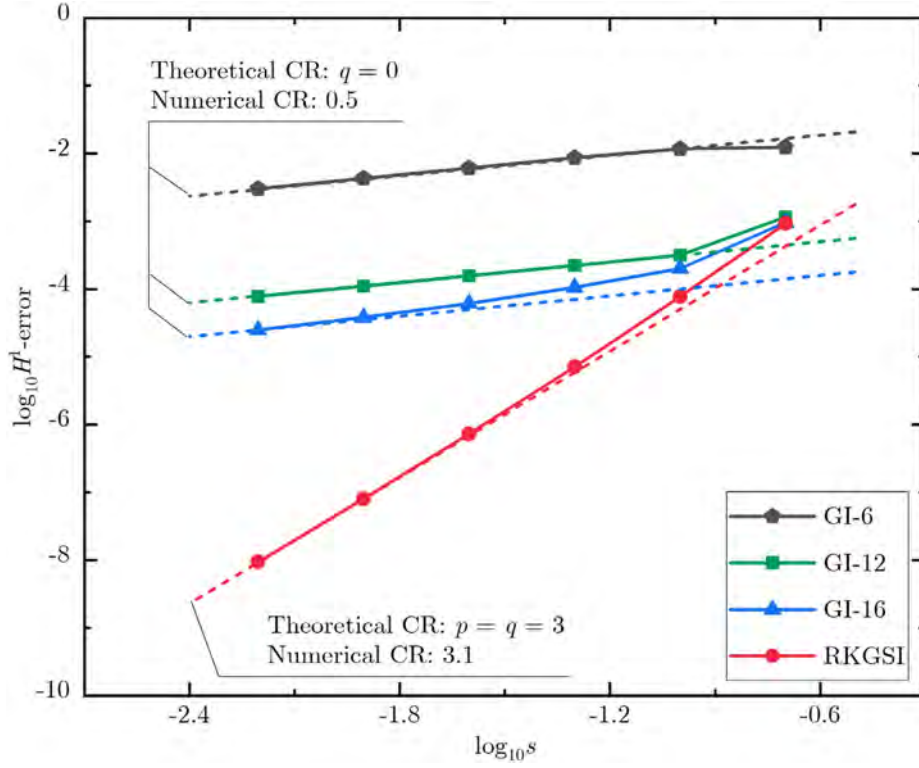


Fig. 17. H^1 -error convergence comparison for the 2D square domain potential problem using cubic meshfree formulation.

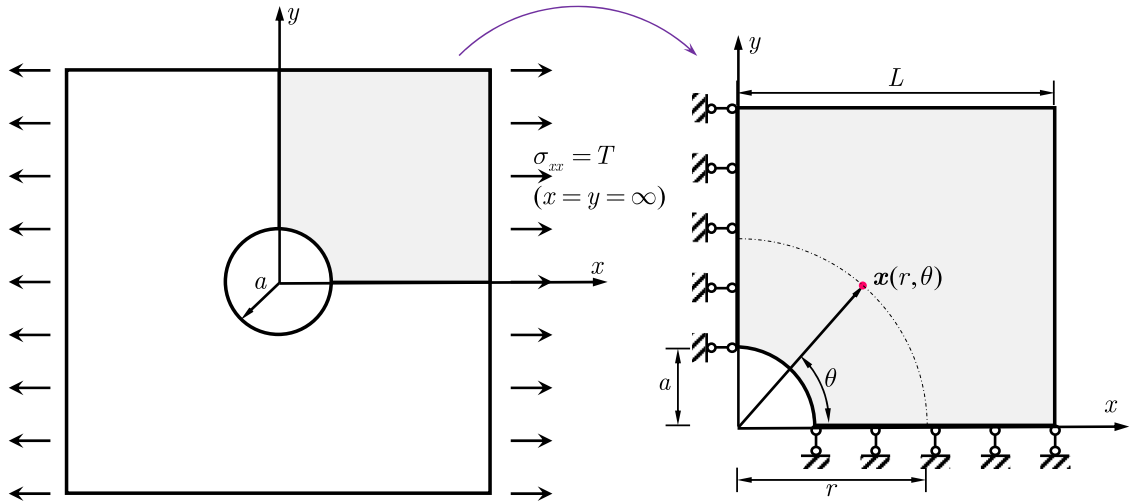


Fig. 18. Description of the elastic plate with a circular hole problem.

conditions are computed according to the following manufactured exact solution:

$$u(\mathbf{x}) = \sin\left(\pi \frac{r - r_i}{r_o - r_i}\right) \cos\left(\pi \frac{z}{L}\right) \quad (75)$$

This 3D hollow cylinder potential problem is analyzed by the cubic meshfree formulation with non-uniform meshfree discretizations of 225, 637, 1377, 4225 and 9537 nodes, and Fig. 29 lists the first three discretizations.

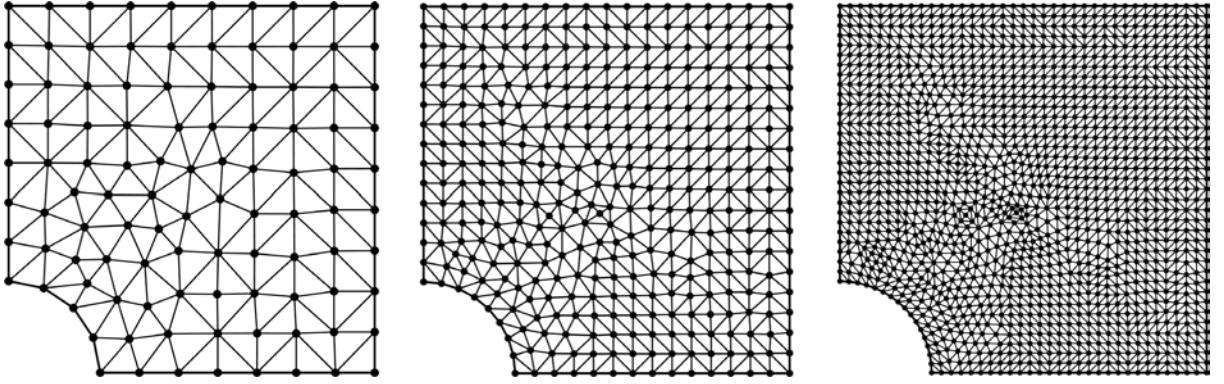


Fig. 19. Meshfree discretizations for the elastic plate with a circular hole problem: 104, 362 and 1373 nodes.

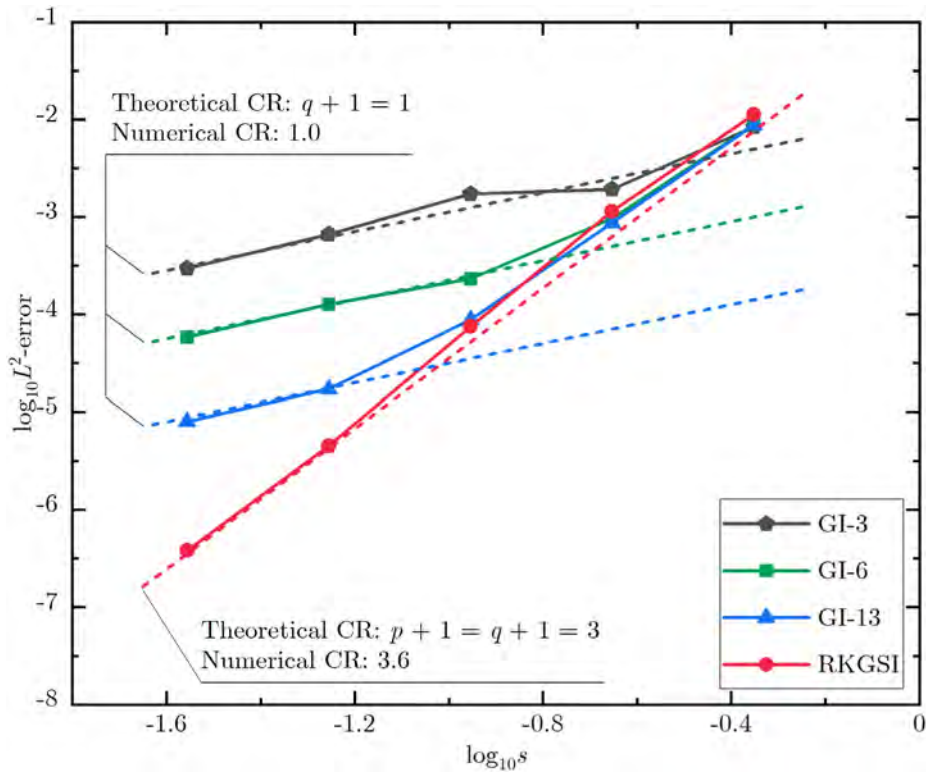


Fig. 20. L^2 -error convergence comparison for the elastic plate with a circular hole problem using quadratic meshfree formulation.

The normalized support size of cubic meshfree shape functions is set to be 3.1. The convergence results for L^2 and H^1 errors are depicted in Figs. 30 and 31. It can be clearly seen that the convergence rates of GI's are far below the optimal convergence rates, namely, 4 for the L^2 -error and 3 for the H^1 -error. Once again, the results produced by GI-11, GI-14 and GI-20 show the same convergence trends as the meshfree models are progressively refined, which agree with the theoretical results stated in Table 1 and further assert that the convergence characteristics of meshfree formulation with GI's are deteriorated by the integration error. Meanwhile, the theoretically expected optimal convergent rates for L^2 and H^1 errors are congruently produced by RKGSi for this 3D hollow cylinder potential problem using non-uniform meshfree discretizations.

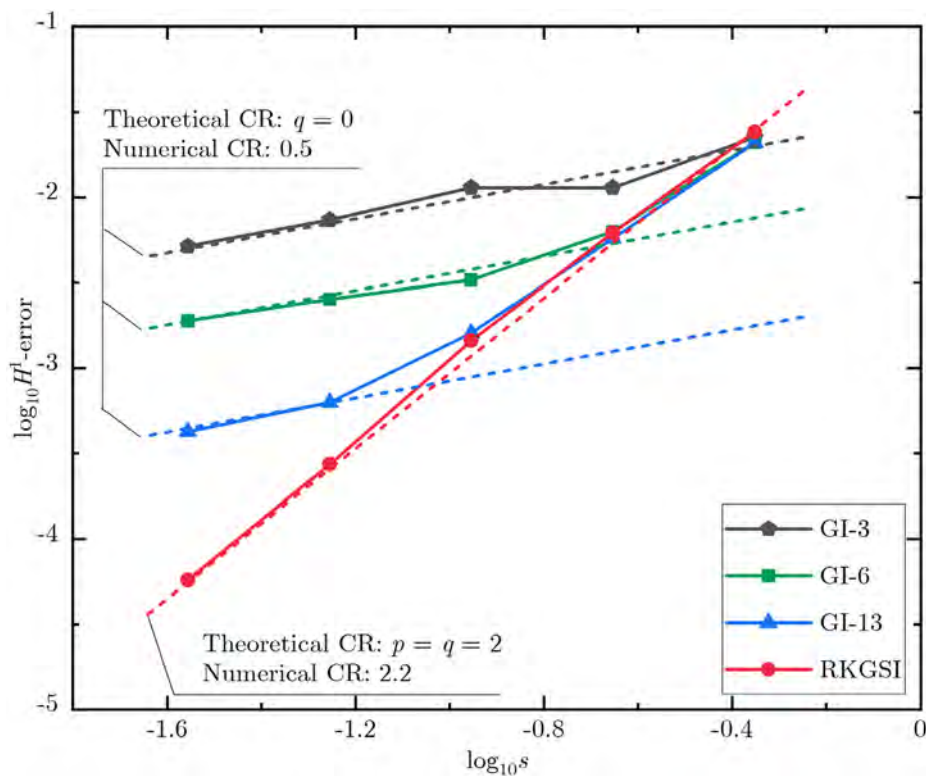


Fig. 21. H^1 -error convergence comparison for the elastic plate with a circular hole problem using quadratic meshfree formulation.

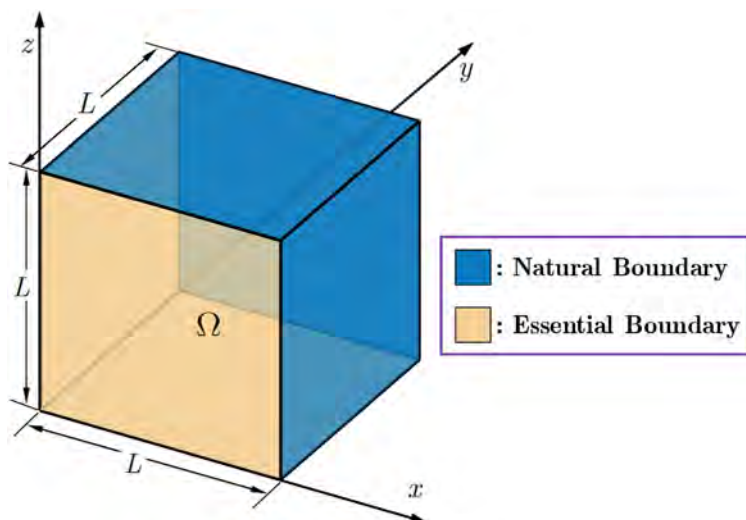


Fig. 22. Description of the 3D cubic domain potential problem.

6. Conclusions

An accuracy analysis of Galerkin meshfree methods was presented to particularly account for the numerical integration effect. It was noted that the integration difficulty of Galerkin meshfree methods leads to a loss of the Galerkin orthogonality condition that is fundamental to develop the error estimates of Galerkin formulation. In order to rationally establish the error estimates for Galerkin meshfree methods, an error measure was proposed

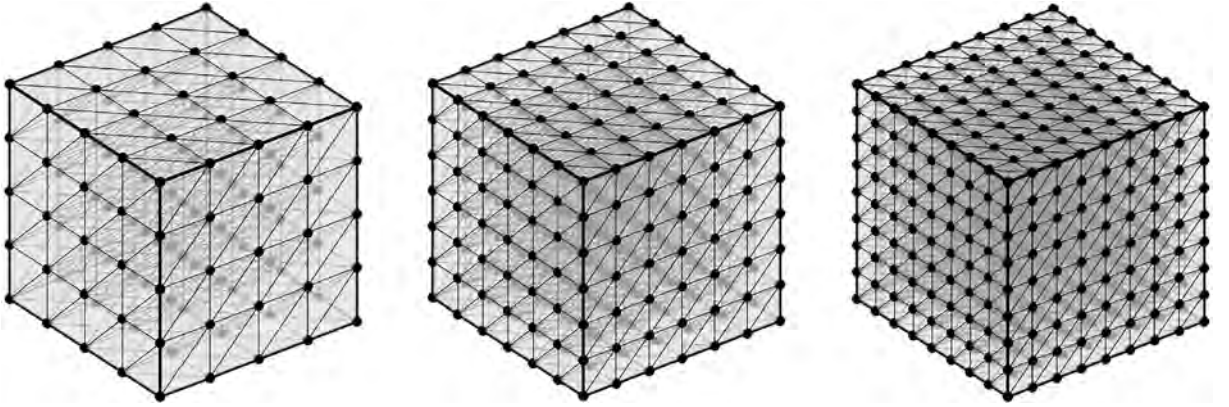


Fig. 23. Meshfree discretizations for the 3D cubic domain potential problem: 125, 343 and 729 nodes.

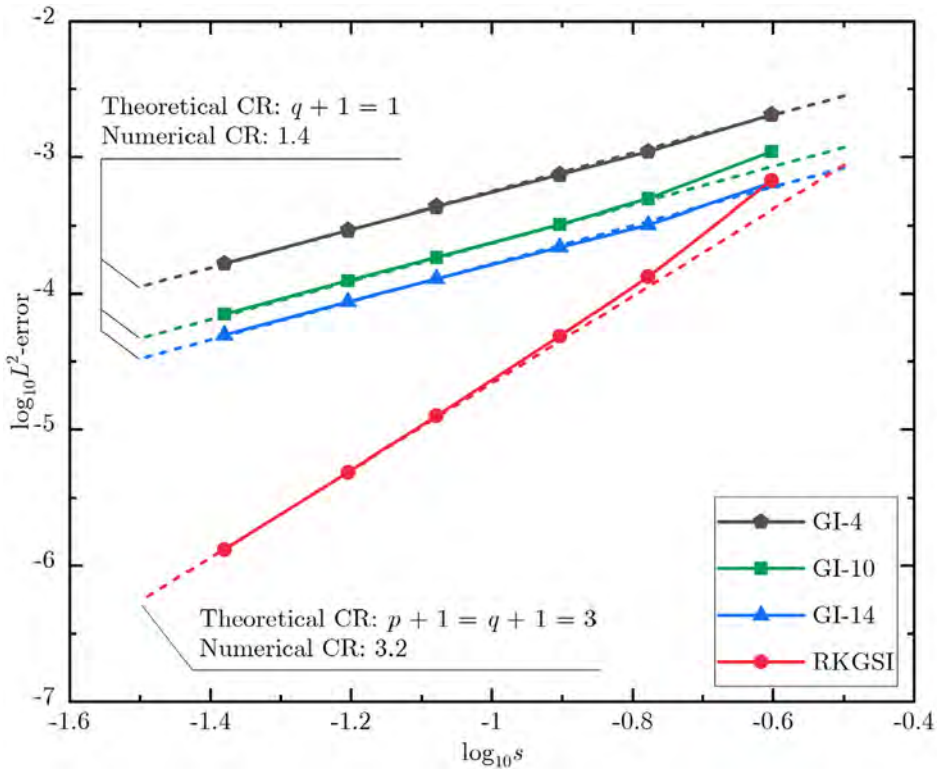


Fig. 24. L^2 -error convergence comparison for the 3D cubic domain potential problem using quadratic meshfree formulation.

to evaluate the error resulting from the loss of Galerkin orthogonality. It was proved that the error arising from the Galerkin orthogonality is dependent on the order of integration consistency of Galerkin meshfree formulation. Subsequently, based upon the error estimate of Galerkin orthogonality, both L^2 and H^1 error estimates incorporating the numerical integration effect were developed for Galerkin meshfree methods, which disclosed that the error estimates of Galerkin meshfree methods are closely related with the numerical integration.

More specifically, the L^2 and H^1 error estimates of Galerkin meshfree formulation are formed by two components, one originates from the standard interpolation error that depends on the degree of meshfree basis functions, and another one attributes to the integration error that relies on the order of integration consistency. Consequently, the overall solution accuracy of Galerkin meshfree methods is controlled by the interplay between the interpolation

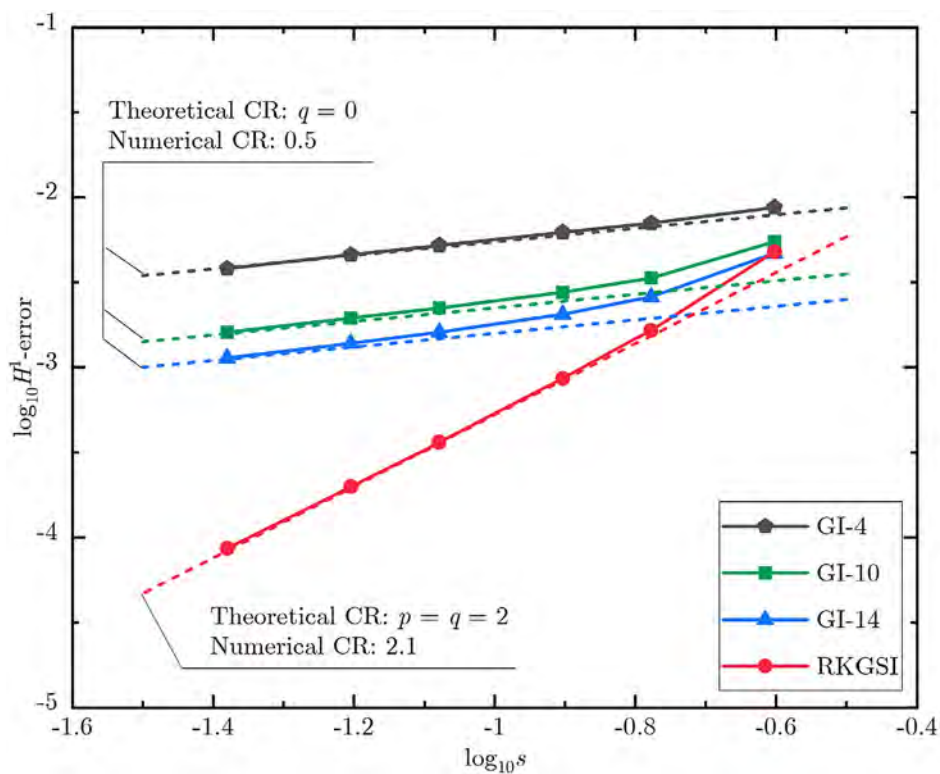


Fig. 25. H^1 -error convergence comparison for the 3D cubic domain potential problem using quadratic meshfree formulation.

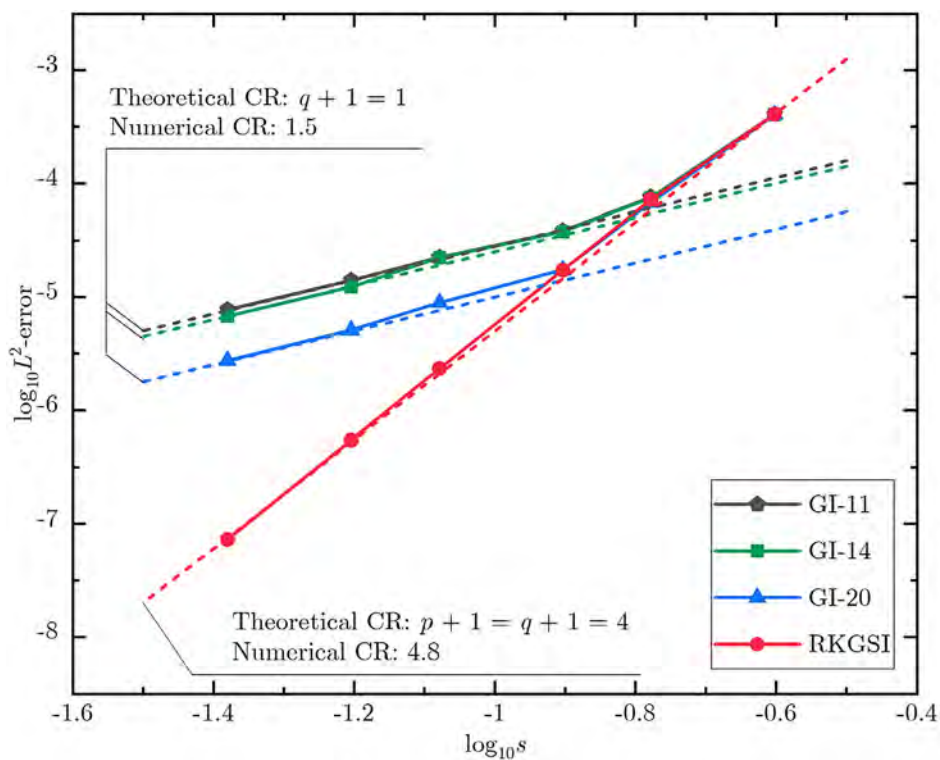


Fig. 26. L^2 -error convergence comparison for the 3D cubic domain potential problem using cubic meshfree formulation.

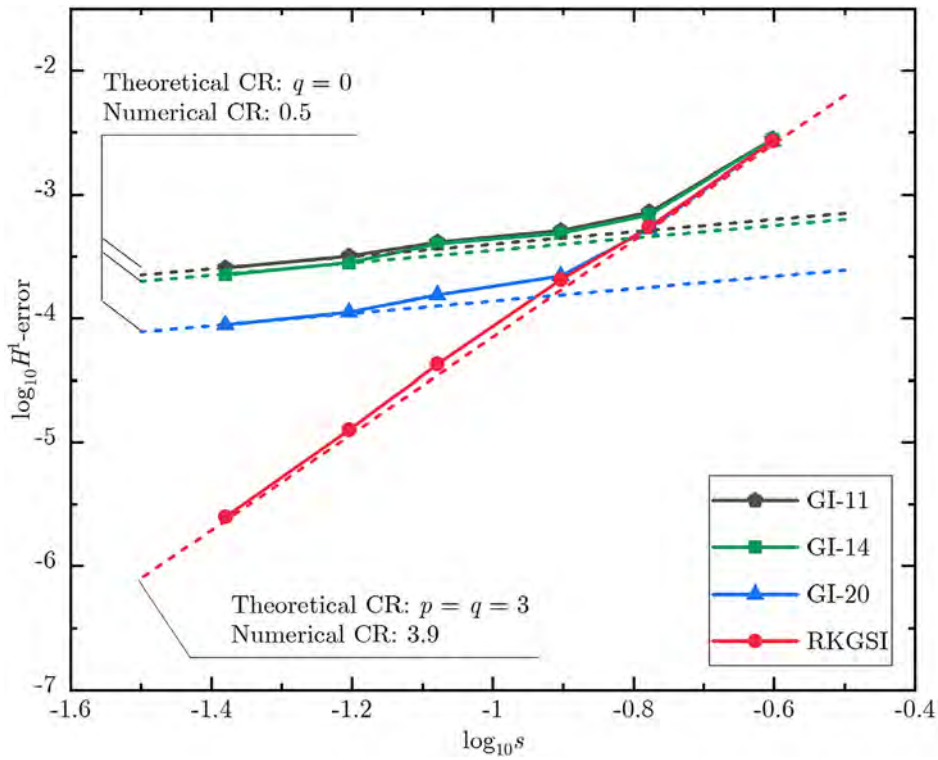


Fig. 27. H^1 -error convergence comparison for the 3D cubic domain potential problem using cubic meshfree formulation.

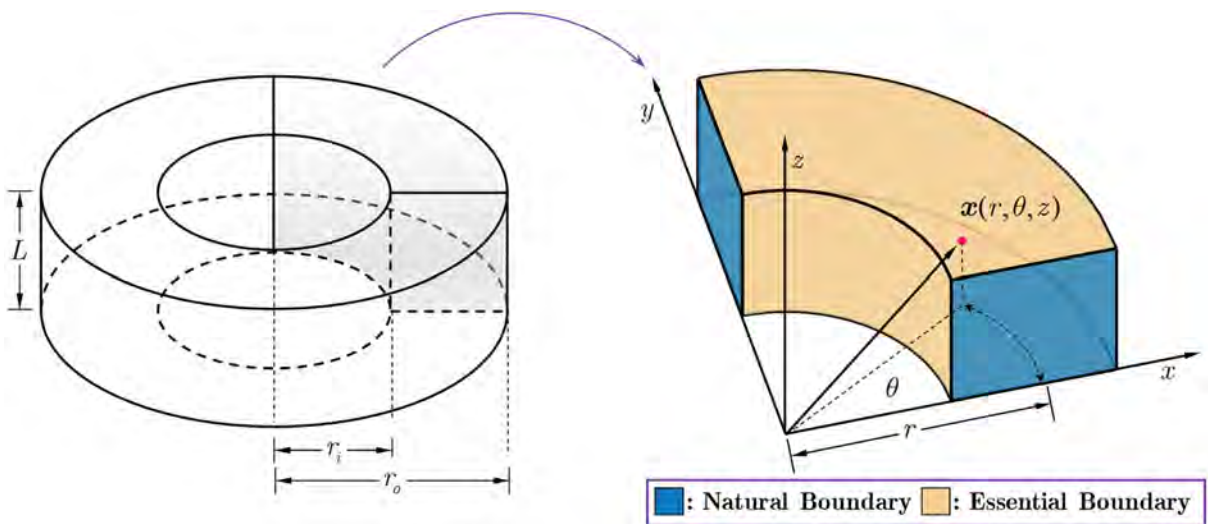


Fig. 28. Description of the 3D hollow cylinder potential problem.

error and integration error. It was theoretically shown that for the integration schemes which do not fulfill any order of integration consistency, for example, the conventional Gauss integration, the accuracy of Galerkin meshfree formulation is eventually determined by the integration error, and an increase of quadrature points will not be able to improve the convergence behaviors. On the other hand, if consistent integration algorithms are used, e.g., the reproducing kernel gradient smoothing integration, the interpolation and integration errors have the same

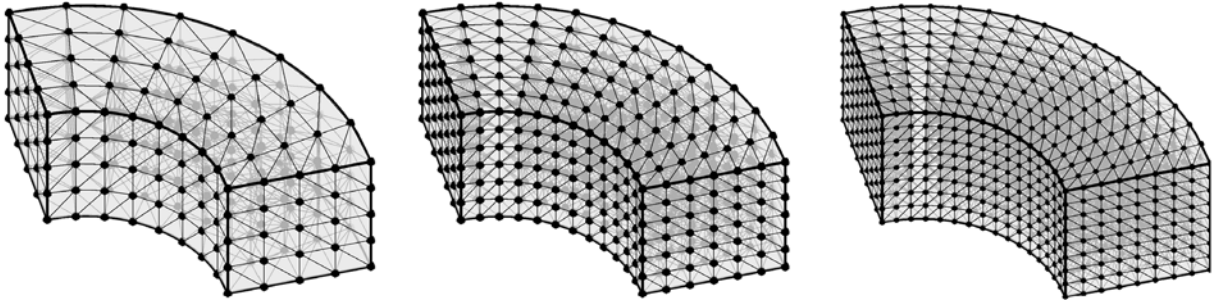


Fig. 29. Meshfree discretizations for the 3D hollow cylinder potential problem: 66, 231 and 861 nodes.

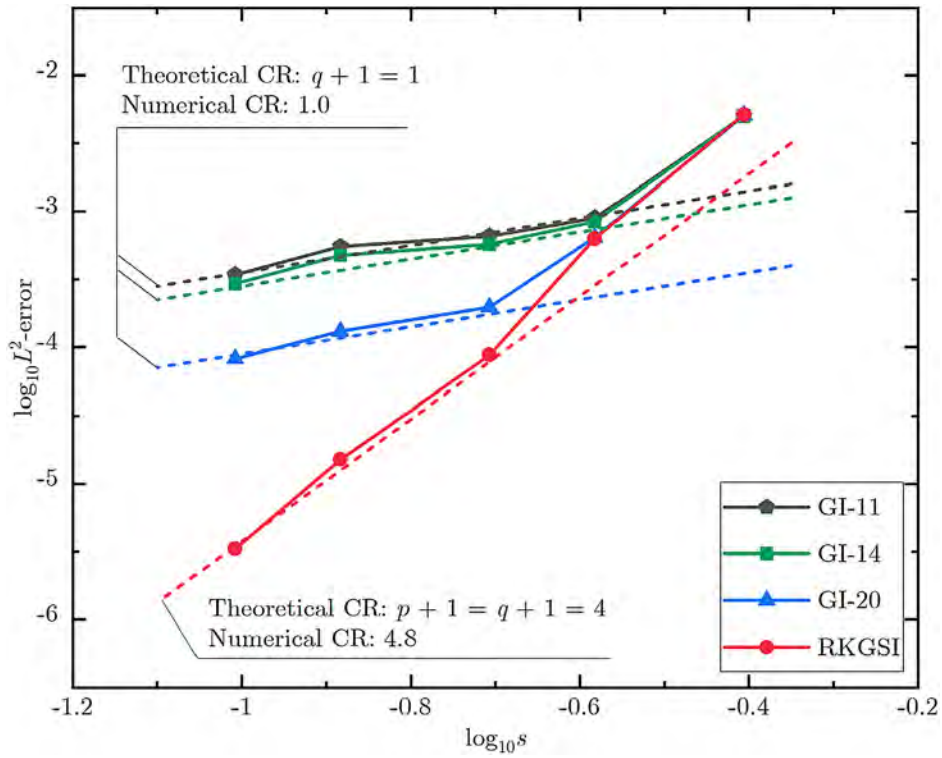


Fig. 30. L^2 -error convergence comparison for the 3D hollow cylinder potential problem using cubic meshfree formulation.

accuracy orders, optimal convergence rates are then ensured for Galerkin meshfree solutions. Numerical results well demonstrated the validity of the proposed theoretical error estimates for Galerkin meshfree methods.

Declaration of competing interest

The authors declare that they have no known competing financial interests or personal relationships that could have appeared to influence the work reported in this paper.

Acknowledgments

The support of this work by the National Natural Science Foundation of China (11772280, 12072302) and the Scientific Research Funds of Huaqiao University (20BS110) is gratefully acknowledged.

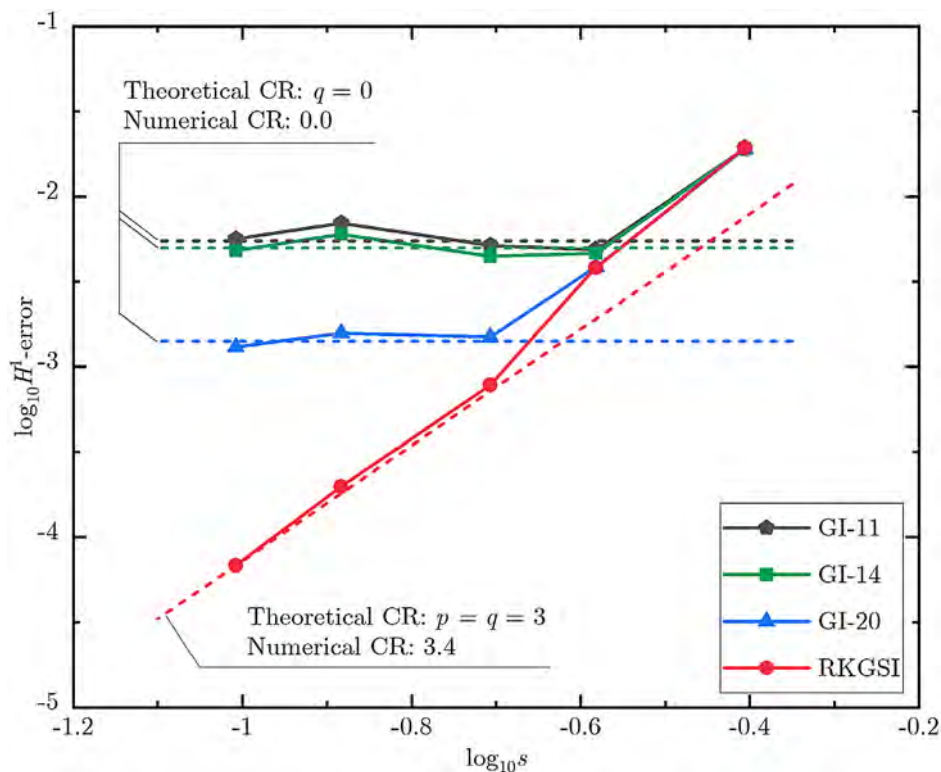


Fig. 31. H^1 -error convergence comparison for the 3D hollow cylinder potential problem using cubic meshfree formulation.

References

- [1] T. Belytschko, Y. Krongauz, D. Organ, M. Fleming, P. Krysl, Meshless methods: an overview and recent developments, *Comput. Methods Appl. Mech. Engrg.* 139 (1996) 3–47.
- [2] S.N. Atluri, S.P. Shen, *The Meshless Local Petrov–Galerkin (MLPG) Method*, Tech Science, 2002.
- [3] I. Babuška, U. Banerjee, J.E. Osborn, Survey of meshless and generalized finite element methods: a unified approach, *Acta Numer.* 12 (2003) 1–125.
- [4] S. Li, W.K. Liu, *Meshfree Particle Methods*, Springer-Verlag, 2004.
- [5] X. Zhang, Y. Liu, *Meshless Methods*, Tsinghua University Press & Springer-Verlag, 2004.
- [6] V.P. Nguyen, T. Rabczuk, S. Bordas, M. Duflot, Meshless methods: A review and computer implementation aspects, *Math. Comput. Simulation* 79 (2008) 763–813.
- [7] G.R. Liu, *Meshfree Methods: Moving beyond the Finite Element Method*, second ed., CRC Press, 2009.
- [8] J.S. Chen, M. Hillman, S.W. Chi, Meshfree methods: progress made after 20 years, *J. Eng. Mech. ASCE* 143 (2017) 04017001.
- [9] B. Nayroles, G. Touzot, P. Villon, Generalizing the finite element method: Diffuse approximation and diffuse elements, *Comput. Mech.* 10 (1992) 307–318.
- [10] T. Belytschko, Y.Y. Lu, L. Gu, Element-free Galerkin methods, *Internat. J. Numer. Methods Engrg.* 37 (1994) 229–256.
- [11] T. Belytschko, Y.Y. Lu, L. Gu, M. Tabbara, Element-free Galerkin methods for static and dynamic fracture, *Int. J. Solids Struct.* 32 (1995) 2547–2570.
- [12] W.K. Liu, S. Jun, Y.F. Zhang, Reproducing kernel particle methods, *Internat. J. Numer. Methods Fluids* 20 (1995) 1081–1106.
- [13] J.S. Chen, C. Pan, C.T. Wu, W.K. Liu, Reproducing kernel particle methods for large deformation analysis of nonlinear structures, *Comput. Methods Appl. Mech. Engrg.* 139 (1996) 195–227.
- [14] C.A. Duarte, J.T. Oden, An hp adaptive method using clouds, *Comput. Methods Appl. Mech. Engrg.* 139 (1996) 237–262.
- [15] I. Babuška, J.M. Melenk, The partition of unity method, *Internat. J. Numer. Methods Engrg.* 40 (1997) 727–758.
- [16] N. Sukumar, B. Moran, T. Belytschko, The natural element method in solid mechanics, *Internat. J. Numer. Methods Engrg.* 43 (1998) 839–887.
- [17] S.N. Atluri, T. Zhu, A new meshless local Petrov–Galerkin (MLPG) approach in computational mechanics, *Comput. Mech.* 22 (1998) 117–127.
- [18] J.G. Wang, G.R. Liu, A point interpolation meshless method based on radial basis functions, *Internat. J. Numer. Methods Engrg.* 54 (2002) 1623–1648.

- [19] W.K. Liu, W. Han, H. Lu, S. Li, J. Cao, Reproducing kernel element method. Part I: Theoretical formulation, *Comput. Methods Appl. Mech. Engrg.* 193 (2004) 933–951.
- [20] N. Sukumar, Construction of polygonal interpolants: a maximum entropy approach, *Internat. J. Numer. Methods Engrg.* 61 (2004) 2159–2181.
- [21] M. Arroyo, M. Ortiz, Local maximum-entropy approximation schemes: a seamless bridge between finite elements and meshfree methods, *Internat. J. Numer. Methods Engrg.* 65 (2006) 2167–2202.
- [22] G.R. Liu, K.Y. Dai, T.T. Nguyen, A smoothed finite element method for mechanics problems, *Comput. Mech.* 39 (2007) 859–877.
- [23] P.C. Guan, S.W. Chi, J.S. Chen, T.R. Slawson, M.J. Roth, Semi-Lagrangian reproducing kernel particle method for fragment-impact problems, *Int. J. Impact Eng.* 38 (2011) 1033–1047.
- [24] D. Wang, P. Chen, Quasi-convex reproducing kernel meshfree method, *Comput. Mech.* 54 (2014) 689–709.
- [25] P. Metsis, N. Lantounis, M. Papadrakakis, A new hierarchical partition of unity formulation of EFG meshless methods, *Comput. Methods Appl. Mech. Engrg.* 283 (2015) 782–805.
- [26] E. Yreux, J.S. Chen, A quasi-linear reproducing kernel particle method, *Internat. J. Numer. Methods Engrg.* 109 (2017) 1045–1064.
- [27] Y. Wu, C.T. Wu, Simulation of impact penetration and perforation of metal targets using the smoothed particle Galerkin method, *J. Eng. Mech. ASCE* 144 (2018) 04018057.
- [28] N. Trask, P. Bochev, M. Perego, A conservative, consistent, and scalable meshfree mimetic method, *J. Comput. Phys.* 409 (2020) 109187.
- [29] P. Lancaster, K. Salkauskas, Surfaces generated by moving least squares methods, *Math. Comp.* 37 (1981) 141–158.
- [30] J. Dolbow, T. Belytschko, Numerical integration of the Galerkin weak form in meshfree methods, *Comput. Mech.* 23 (1999) 219–230.
- [31] S. Beissel, T. Belytschko, Nodal integration of the element-free Galerkin method, *Comput. Methods Appl. Mech. Engrg.* 139 (1996) 49–74.
- [32] C.T. Dyka, P.W. Randles, R.P. Ingel, Stress points for tension instability in SPH, *Internat. J. Numer. Methods Engrg.* 40 (1997) 2325–2341.
- [33] T. Rabczuk, T. Belytschko, S.P. Xiao, Stable particle methods based on Lagrangian kernels, *Comput. Methods Appl. Mech. Engrg.* 193 (2004) 1035–1063.
- [34] C.T. Wu, Y. Wu, Z. Liu, D. Wang, A stable and convergent Lagrangian particle method with multiple local stress points for large strain and material failure analysis, *Finite Elem. Anal. Des.* 146 (2018) 96–106.
- [35] M. Hillman, J.S. Chen, An accelerated, convergent, and stable nodal integration in Galerkin meshfree methods for linear and nonlinear mechanics, *Internat. J. Numer. Methods Engrg.* 107 (2016) 603–630.
- [36] R. Silva-Valenzuela, A. Ortiz-Bernardin, N. Sukumar, E. Artioli, N. Hitschfeld-Kahler, A nodal integration scheme for meshfree Galerkin methods using the virtual element decomposition, *Internat. J. Numer. Methods Engrg.* 121 (2020) 2174–2205.
- [37] S. De, K.J. Bathe, The method of finite spheres with improved numerical integration, *Comput. Struct.* 79 (2001) 2183–2196.
- [38] A. Carpinteri, G. Ferro, G. Ventura, The partition of unity quadrature in meshless methods, *Internat. J. Numer. Methods Engrg.* 54 (2002) 987–1006.
- [39] Y. Liu, T. Belytschko, A new support integration scheme for the weakform in mesh-free methods, *Internat. J. Numer. Methods Engrg.* 82 (2010) 699–715.
- [40] J.S. Chen, C.T. Wu, S. Yoon, Y. You, A stabilized conforming nodal integration for Galerkin mesh-free methods, *Internat. J. Numer. Methods Engrg.* 50 (2001) 435–466.
- [41] J.S. Chen, S. Yoon, C.T. Wu, Non-linear version of stabilized conforming nodal integration for Galerkin mesh-free methods, *Internat. J. Numer. Methods Engrg.* 53 (2002) 2587–2615.
- [42] B.M. Irons, A. Razzaque, Experience with the patch test for convergence of finite element methods, in: A.K. Aziz (Ed.), *Mathematical Foundations of the Finite Element Method*, Academic Press, London, 1972, pp. 557–587.
- [43] O.C. Zienkiewicz, R.L. Taylor, The finite element patch test revisited a computer test for convergence, validation and error estimates, *Comput. Methods Appl. Mech. Eng.* 149 (1997) 223–254.
- [44] D. Wang, J.S. Chen, Locking-free stabilized conforming nodal integration for meshfree Mindlin-Reissner plate formulation, *Comput. Methods Appl. Mech. Eng.* 193 (2004) 1065–1083.
- [45] J.S. Chen, D. Wang, A constrained reproducing kernel particle formulation for shear deformable shell in Cartesian coordinates, *Internat. J. Numer. Methods Engrg.* 68 (2006) 151–172.
- [46] D. Wang, J.S. Chen, A Hermite reproducing kernel approximation for thin-plate analysis with sub-domain stabilized conforming integration, *Internat. J. Numer. Methods Engrg.* 74 (2008) 368–390.
- [47] D. Wang, Y. Wu, An efficient Galerkin meshfree analysis of shear deformable cylindrical panels, *Interact. Multiscale Mech.* 1 (2008) 339–355.
- [48] D. Wang, Z. Lin, Dispersion and transient analyses of Hermite reproducing kernel Galerkin meshfree method with sub-domain stabilized conforming integration for thin beam and plate structures, *Comput. Mech.* 48 (2011) 47–63.
- [49] D. Wang, H. Peng, A Hermite reproducing kernel Galerkin meshfree approach for buckling analysis of thin plates, *Comput. Mech.* 51 (2013) 1013–1029.
- [50] D. Wang, C. Song, H. Peng, A circumferentially enhanced Hermite reproducing kernel meshfree method for buckling analysis of Kirchhoff–Love cylindrical shells, *Int. J. Struct. Stab. Dyn.* 15 (2015) 1450090.
- [51] D. Wang, Z. Li, L. Li, Y. Wu, Three dimensional efficient meshfree simulation of large deformation failure evolution in soil medium, *Sci. China Tech. Sci.* 54 (2011) 573–580.
- [52] Y. Wu, D. Wang, C.T. Wu, Three dimensional fragmentation simulation of concrete structures with a nodally regularized meshfree method, *Theor. Appl. Fract. Mech.* 72 (2014) 89–99.

- [53] Y. Wu, D. Wang, C.T. Wu, H. Zhang, A direct displacement smoothing meshfree particle formulation for impact failure modeling, *Int. J. Impact Eng.* 87 (2016) 169–185.
- [54] D. Wang, J. Wang, J. Wu, J. Deng, M. Sun, A three dimensional two-level gradient smoothing meshfree method for rainfall induced landslide simulations, *Front. Struct. Civ. Eng.* 13 (2019) 337–352.
- [55] X.F. Pan, C.T. Wu, W. Hu, Y. Wu, A momentum-consistent stabilization algorithm for Lagrangian particle methods in the thermo-mechanical friction drilling analysis, *Comput. Mech.* 64 (2019) 625–644.
- [56] T.H. Huang, J.S. Chen, H. Wei, M. Roth, E.H. Fang, A MUSCL-SCNI approach for meshfree modeling of shock waves in fluids, *Comput. Part. Mech.* 7 (2020) 329–350.
- [57] Q. Duan, X. Li, H. Zhang, T. Belytschko, Second-order accurate derivatives and integration schemes for meshfree methods, *Internat. J. Numer. Methods Engrg.* 92 (2012) 399–424.
- [58] Q. Duan, X. Gao, B. Wang, X. Li, H. Zhang, T. Belytschko, Y. Shao, Consistent element-free Galerkin method, *Internat. J. Numer. Methods Engrg.* 99 (2014) 79–101.
- [59] B. Wang, C. Lu, C. Fan, M. Zhao, Consistent integration schemes for meshfree analysis of strain gradient elasticity, *Comput. Methods Appl. Mech. Engrg.* 357 (2019) 112601.
- [60] J.S. Chen, M. Hillman, M. Rüter, An arbitrary order variationally consistent integration for Galerkin meshfree methods, *Internat. J. Numer. Methods Engrg.* 95 (2013) 387–418.
- [61] M. Hillman, J.S. Chen, S.W. Chi, Stabilized and variationally consistent nodal integration for meshfree modeling of impact problems, *Comput. Part. Mech.* 1 (2014) 245–256.
- [62] D. Wang, J. Wu, An efficient nesting sub-domain gradient smoothing integration algorithm with quadratic exactness for Galerkin meshfree methods, *Comput. Methods Appl. Mech. Engrg.* 298 (2016) 485–519.
- [63] D. Wang, J. Wu, An inherently consistent reproducing kernel gradient smoothing framework toward efficient Galerkin meshfree formulation with explicit quadrature, *Comput. Methods Appl. Mech. Engrg.* 349 (2019) 628–672.
- [64] J. Wu, D. Wang, Z. Lin, D. Qi, An efficient gradient smoothing meshfree formulation for the fourth-order phase field modeling of brittle fracture, *Comput. Part. Mech.* 7 (2020) 193–207.
- [65] G. Strang, Variational crimes in finite element method, in: A.K. Aziz (Ed.), *The Mathematical Foundations of the Finite Element Method with Applications to Partial Differential Equations*, Academic Press, 1972, pp. 689–710.
- [66] G. Strang, G. Fix, *An Analysis of the Finite Element Method*, Wellesley-Cambridge Press, 2018.
- [67] W.K. Liu, Y. Chen, C.T. Chang, T. Belytschko, Advances in multiple scale kernel particle methods, *Comput. Mech.* 18 (1996) 73–111.
- [68] W.K. Liu, S. Li, T. Belytschko, Moving least-square reproducing kernel methods (I) methodology and convergence, *Comput. Methods Appl. Mech. Engrg.* 143 (1997) 113–154.
- [69] J.S. Chen, W. Han, Y. You, X. Meng, A reproducing kernel method with nodal interpolation property, *Internat. J. Numer. Methods Engrg.* 56 (2003) 935–960.
- [70] W. Han, X. Meng, Error analysis of the reproducing kernel particle method, *Comput. Methods Appl. Mech. Engrg.* 190 (2001) 6157–6181.
- [71] I. Babuška, U. Banerjee, J.E. Osborn, Q. Li, Quadrature for meshless methods, *Internat. J. Numer. Methods Engrg.* 76 (2008) 1434–1470.
- [72] M. Rüter, J.S. Chen, An enhanced-strain error estimator for Galerkin meshfree methods based on stabilized conforming nodal integration, *Comput. Math. Appl.* 74 (2017) 2144–2171.
- [73] S. Fernández-Méndez, A. Huerta, Imposing essential boundary conditions in mesh-free methods, *Comput. Methods Appl. Mech. Engrg.* 193 (2004) 1257–1275.
- [74] A. Quarteroni, A. Valli, *Numerical Approximation of Partial Differential Equations*, Springer, 1994.
- [75] R.L. Burden, J.D. Faires, *Numerical Analysis*, 9th ed., Brooks Cole, 2010.
- [76] P.J. Davis, P. Rabinowitz, *Methods of Numerical Integration*, Courier Corporation, 2007.
- [77] G. Philippe, *Linear and Nonlinear Functional Analysis with Applications*, SIAM-Society for Industrial and Applied Mathematics, 2013.
- [78] T.J.R. Hughes, *The Finite Element Method: Linear Static and Dynamic Finite Element Analysis*, Dover Publications, 2000.
- [79] O.C. Zienkiewicz, R.L. Taylor, J.Z. Zhu, *The Finite Element Method: Its Basis and Fundamentals*, 7th ed., Elsevier, Singapore, 2015.
- [80] S.P. Timoshenko, J.N. Goodier, *Theory of Elasticity*, third ed., McGraw-Hill, 1970.